Combined application of distributed fibre optical and digital image correlation measurements to structural concrete experiments

by Jaime Mata-Falcón*, Severin Haefliger, Minu Lee, Tena Galkovski and Nicola Gehri

Institute of Structural Engineering, ETH Zurich, Switzerland

*Corresponding author, Stefano-Franscini-Platz 5, 8093 Zurich, Switzerland, email: mata-falcon@ibk.baug.ethz.ch

Published in:

Journal: Engineering Structures; Volume 225, 15 December 2020, 111309

https://doi.org/10.1016/j.engstruct.2020.111309

Keywords

concrete structures; experimental measurements; photogrammetry; digital image correlation; distributed fibre optical strain sensing

Abstract

The combined application of distributed fibre optical strain measurements on reinforcing bars and digital image correlation (DIC) measurements on the concrete surface has a great potential to increase knowledge in many fields of structural concrete. This paper explores the advantages of these measurement techniques for concrete tests and the key aspects to be considered in order to obtain reliable measurements suitable for quantitative analysis. The uncertainty of DIC analysis is highly dependent on the test conditions and user carefulness, and should be assessed for each test. A procedure to quantify the DIC uncertainty in large scale structural tests is presented, showing that it is highly dependent on the quality of the calibration. Comparative tests on distributed fibre optical strain measurements with different fibre coatings show that polyimide-coated fibres capture properly high strain gradients and, therefore, should be used when instrumenting reinforcing bars in RC specimens. Moreover, the measuring noise was found to be dependent on the absolute strain level. Combined plots of crack kinematics and reinforcement strains, stresses and forces are shown for the results of a series of two concrete panel tests subjected to diagonal tension. Crack locations predicted by both measurements match perfectly in these experiments.

1 Introduction

The knowledge in structural concrete is perfectly developed for the dimensioning of new structures using conventional reinforcement and construction methods. Such structures can be designed to provide sufficient deformation capacity (i.e. by ensuring that failure is governed by yielding of the reinforcement) in order to guarantee a safe application of lower bound limit analysis methods [1,2]. However, there is a rising need and interest in the assessment of existing structures as well as in the use of non-conventional reinforcement (e.g. textile and fibre reinforcement) and digital fabrication methods [3,4], for which limit analysis often is not applicable. Therefore, the development of sound mechanical models for existing structures and non-conventional materials is key to avoid unnecessary retrofitting measures and to open the way for the design of leaner new structures. Many such mechanical models have already been proposed for conventional reinforcement [5,6], fibre reinforcement [7,8] and even textile reinforcement [9], but all have been derived based on experiments with very limited directly measured information (typically only loads and deflections, sometimes average strains). Due to this limitation, existing models are prone to containing inconsistencies and/or empirical factors only applicable for the particular case they were derived [10], what hinders their practical application. Novel instrumentation techniques, such as optical systems, allowing distributed measurements on the surface of, and inside the concrete will be essential for the validation and further development of these models. These novel technologies complement standard measurement technologies providing insight into the mechanical behaviour of structural concrete (in particular the kinematics) that hardly has been possible up to now.

Most structural concrete experiments conducted in the past were instrumented using standard measurement technologies. These standard measurements consisted of load-cells to measure applied loads or reactions, and linear displacement sensors (e.g. LVDTs, potentiometers and strain gauge based sensors) to measure selected deflections and average deformations between two points. Strain gauges were sometimes used as well to record strains on reinforcing bars and on the concrete surface, but only a limited number of points could be instrumented (not only because of cost reasons, but also because sensors affect bond behaviour and change the member's characteristic behaviour when applied to reinforcing bars). Moreover, discrete strain measurements on reinforcing bars provide information of limited practical use unless the gauges are located exactly at a crack (which cannot be ensured when placing them except in very particular cases [11]). Using these standard measurement techniques it was possible to determine the load-deformation behaviour and to estimate the global failure mode of the tested members. While this information was sufficient for developing design approaches based on the lower bound limit analysis, knowing more detailed information is essential to fully understand the behaviour of elements with low deformation capacity (e.g. members with very low transversal reinforcement ratios, or with non-conventional reinforcement of limited ductility).

Driven by the impossibility to gather detailed information in real-life structural members, researchers developed simplified test setups to study isolated structural phenomena matching the limitations of existing instrumentation. For instance, aggregate interlock relationships were derived typically based on push-off tests [12], bond relationships from pull-out experiments [13] and tension-stiffening mostly from direct tension or pure bending tests [14]. While these derivations provide valuable insight into these phenomena, there remains an uncertainty about their validity when applied for conditions different than those for which they were derived. For example, aggregate interlock relationships derived in push-off experiments with preformed cracks and theoretical uniform crack openings [15], might not be representative for members containing real cracks with significant macro-roughness and non-uniform crack openings. Therefore, the implementation of empirical relationships derived from simple tests into mechanical models with a general scope is prone to potential inconsistencies [10,16]. To avoid these inconsistencies, refined measurements of non-oversimplified tests representing real-life structures are essential.

Some early attempts in this direction include the use of photoelasticity to quantify the strain field and visualise the cracking pattern [17] or the visual inspection of cracks on the concrete surface. The latter is still the most popular refined measurement nowadays, in which crack patterns are marked by eye inspection and the width of selected cracks is estimated by visual comparison with printed line-widths. The tendency to measure the widest cracks might bias the statistical results obtained with this approach. A more precise measurement consists in tracking the variation of distance between metallic targets glued to the concrete surface by means of a demountable mechanical strain gauge (DEMEC) [18]. Besides crack opening, this procedure also measures compressive strains and crack sliding (provided a grid of triangular targets is tracked), enabling an advanced analysis based on the experimental results (e.g. estimation of the contribution of the different shear-transfer actions [19]). However, all these methods (i) are labour-intensive and error-prone (many manual measurements are required at each measuring step), (ii) only provide discrete information for the concrete surface at certain load steps, and (iii) often cannot be used close to failure due to safety reasons. As discussed in this paper, recent advances in optical measuring techniques overcome these limitations and are therefore replacing rapidly these classical measuring techniques (considered as state-of-the-art until very recently).

The present work addresses the potential of combining in structural concrete experiments two of these novel technologies, i.e. full field digital image correlation (DIC) and distributed fibre optical strain sensing, as schematically illustrated in Figure 1. These instrumentations are able to monitor crack kinematics and concrete strains on the concrete surface and strains along reinforcing bars quasi-continuously (in time and space) without disturbing the structural behaviour of the specimens: DIC measurements are contactless and fibre optics uses tiny glass fibres as sensors with negligible impact on bond. The recorded results allow determining the internal flow of forces of the specimens, as shown in this paper for a series of panel tests. Moreover, the forces transferred across cracks can be obtained directly from equilibrium at the crack locations. An important challenge when using these instrumentation methods lies in the large amount of collected data. This can be overcome by developing tools to automatically transform the acquired data into useful structural information. It should be noted that the knowledge on the accuracy of these technologies and the dependency of the results on the application conditions is still very limited, despite of their potential and their increasing use in structural concrete experiments (particularly for the case of DIC). This uncertainty compromises the reliability of the results except for qualitative interpretations. To improve this situation, several tests to estimate the measurement uncertainty of DIC and fibre optics when applied to large scale structural concrete experiments are discussed in this paper.

2 Distributed optical instrumentation

2.1 Digital image correlation

Digital image correlation (DIC) is a novel but already well-established optical method that allows tracking the displacements of a surface based on pattern matching of digital images [20]. This paper focuses in stereoscopic applications of DIC (3D-DIC), which provide three-dimensional displacements as well as the shape of the surface, which allows avoiding errors due to out-of-plane displacements inherent to two-dimensional DIC (2D-DIC) applications with a single camera. Measuring with DIC comprises the following main steps: (i) acquiring digital images during a test, (ii) tracking displacements between acquired images and (iii) transforming the image displacements in real displacements of the tested member by using a model of the system. Typically, the strain field is computed from the measured displacement field over a certain length (virtual gauge length) in post-processing.

In Step (ii), when tracking pixel displacements in images, unique correlation areas known as subsets or facets (which typically range in size from 10 to 30 square pixels for speckled surfaces) are defined in the reference images (usually the undeformed state). The centre of each subset is a measurement point that is tracked in each successive pair of images (deformed state) using image correlation algorithms. Remarkable progress in the field of image matching has led to current correlation algorithms being quite accurate and insensitive to lighting variations or distortions of the subset. These algorithms provide sub-pixel accuracy by using interpolation filters to reconstruct grey values at non-integer locations (i.e. in between two pixels). The measured surface is typically speckled in order to minimise the noise of the subset correlation to around 1/100 of a pixel, a value typically reported by DIC software manufacturers. The ideal speckle size is 2 to 5 pixels. Smaller speckles might cause aliasing effects and should be avoided; larger speckles would require increasing the subset size to keep the same precision in the correlation, but will reduce the spatial resolution of the measurement. While a measurement point can be set at every single pixel, results of consecutive pixels are not independent as the respective subsets will almost be identical. Therefore, it is common practice to space the measuring points in the range of 1/2 to 1/3 of the subset size for standard applications [21], but a lower spacing might be convenient when using automated crack measurement procedures. The spacing between measuring points is thereafter referred to as step size.

Once the displacements (in pixels) in each measuring point have been tracked for all images, this information is translated into global coordinates by using an appropriate model of the optical system, based on photogrammetry principles. The optical system is characterised by internal parameters for each of the two cameras and by external parameters, which have to be calibrated for each measurement. The internal parameters comprise the focal length and parameters to correct the effect of lens distortions or skewed sensors. The external parameters include the translations and displacements between the cameras. Bundle adjustment is the most common calibration technique for 3D-DIC applications. It is suitable for complex optical systems and typically consists in the acquisition of a number of images of a calibration target that has fiducial points (e.g. circle markers or checkerboard), in which at least one distance between two fiducial points has to be accurately known to determine the scale factor. In the following, this is referred to as standard calibration. The standard calibration can be refined with the information of several images of a speckled non-deformable object (also known as hybrid calibration) [22].

DIC has found widespread use in recent years in structural engineering experimentation thanks to its versatility. The possibility of measuring full field information of the tested members and of freely extracting the key information (cracking behaviour) in the post-processing phase brings research on structural concrete to a new dimension. This potential has already been exploited in recent studies when measuring critical shear cracks [23,24]. However, in spite of its benefits, there are some key aspects to be considered when using digital image correlation for structural concrete applications:

- The measurement uncertainty is highly dependent on the hardware configuration (2D-DIC or 3D-DIC, quality of the cameras, etc.) and the test setup, but especially on the user care and expertise. The value of 1/100 of a pixel for the system accuracy typically provided by manufactures is only representative for the measurement uncertainty under perfect conditions. Therefore, the measurement uncertainty should be estimated and reported independently for every measurement.
- The calibration has a large impact on the measurement uncertainty. Moreover, an accurate calibration for large scale structural tests is often very challenging. This aspect is discussed in Section 3.1, where the

influence of different calibration procedures on the measurement uncertainty of large scale tests is presented.

- There are no standardised procedures yet to estimate the measurement uncertainty of digital image correlation in large scale structural tests. To overcome this unsatisfactory situation, several procedures applicable for large scale tests are presented and discussed in Section 3.1.
- The large amount of produced data requires developing specific processing tools to extract condensed, unbiased and useful information in an efficient way. To tackle this issue the authors have developed a software for the automated crack detection and measurement (called ACDM [25]), which is applied to the experimental tests presented in Section 4. The basic concept of ACDM is described in Section 4.2.

2.2 Fibre optical strain sensing

Fibre optical strain sensing is based on the analysis of the backscatter of light travelling through an optical fibre. A local change in temperature or strain of the fibre results in an alteration of its backscatter properties, which can then be used to detect the location and magnitude of this change. The light is backscattered either at artificial distortions in the fibre (e.g. inscribed Bragg gratings along the fibre) or at natural local defects of the fibre glass itself, such as the variation of the refractive index. Natural local defects generate Raman, Brillouin and Rayleigh backscatter, which can be used for temperature sensing (Raman) or for either temperature or strain sensing (Brillouin and Rayleigh) [26]. While an optical time domain analysis of the Brillouin backscatter allows measuring strains over tens of kilometres with a sensor spacing of about one meter, an optical frequency domain analysis of the Rayleigh backscatter increases the spatial resolution up to 1 mm for a maximum sensing length of about 50 m with a sensitivity of only a few µm/m [26,27]. Therefore, Rayleigh based strain sensing systems are very promising for structural concrete applications as they allow measuring strains quasi-continuously with an adequate precision. Strain sensing systems based on Rayleigh backscatter consist of a laser with variable tuneable frequency coupled to a Mach-Zehnder interferometer [27,28]. The backscattered light from a sensing fibre interacts with the signal of a reference fibre with constant length placed inside the interferometer. The superimposed signal is then analysed by a detector. The varying wavelength of the laser leads to a periodic interference signal, whose frequencies can be obtained by applying a fast Fourier transform. A specific detected frequency of certain intensity corresponds to the backscatter of a specific fibre segment. The farther away the segment is from the source, the higher the frequency of the interference signal. For a fibre in steady environment, the interference signal stays constant. When applying a strain to a certain fibre segment, the corresponding frequency of this and any following segment is shifted proportionally to the applied strain.

Single mode fibres with a glass core of diameter 5 to 9 μm are normally used as sensors. The core of fibres made for telecom applications is mostly optimised to keep backscatter and therefore signal loss low, whereas for sensing fibres a certain amount of backscatter is desired. A surrounding cladding of typically diameter 125 μm, with different refractive index, keeps the light traveling inside the core. Most often a coating made of acrylate, polyimide, nylon or other material surrounds the cladding to protect the bare glass. Depending on the application, this protection might be complemented with further coating layers [29,30]. The bare or coated fibre is applied to the measuring element, e.g. by gluing on the element or – for concrete elements – by placing inside the formwork before casting. Depending on the product, the price per metre fibre length varies between a few Cents and several Euros, which nevertheless contrasts the high investment costs for the reflectometer.

The choice of the appropriate sensing fibre depends on its application. When glued on the concrete surface, fibres coated by soft layers should be used, as the soft coating allows the fibre to slip protecting it from breaking due to the high deformations in the vicinity of the crack. While this application is mainly used for qualitative measurements in structural concrete, e.g. for detecting the location of cracks, approaches to compute the crack width out of the measured fibre strains have also been derived [31]. For quantitative strain sensing of a material without discontinuities, e.g. of reinforcing bars, a proper shear transfer between the different layers cladding – coating(s) – glue – object is decisive [32,33]. In case of a low shear stiffness of the layers or even slip between them, the strain variations might be compromised (i.e. underestimation of strains close to a local maximum and overestimation of strains close to a local minimum). This issue is critical and will be analysed in Section 3.2.3. Fibres with a rigid coating (e.g. polyimide) that are rigidly bonded onto an object without or with very limited strain localisation (e.g. cold-stretched reinforcing bars), allow to reliably measure the strain along the instrumented length when glued with an appropriate adhesive. However, it should be noted that the use of fibres containing very stiff coating materials (i.e. overall stiffness not negligible compared to the stiffness of the monitored object, as is the case of coatings with metal inlays) might bias the results since it is acting as reinforcement. Regarding the suitability of an adhesive, besides an easy handling, a proper shear transfer should be ensured by means of a sufficient shear stiffness and a sufficient shear resistance at the interface. The shear stiffness can be estimated by the shear modulus $G = E/(2(1+\nu))$ (which depends on Young's modulus E and Poisson ratio ν), while the shear resistance depends on the bulk material and is typically given by the manufacturer.

It should be outlined that fibre optical strain sensing is not suitable to measure plastic strains of materials that undergo a pronounced strain localisation when yielding (so called Lüders bands for metals). This is e.g. the case for hot-rolled, quenched and self-tempered steels, of which a major part of todays used reinforcing bars consists [34–36]. When yielding, these steels stretch locally up to 20'000 μm/m, whereas the maximum detectable strain range of commercial reflectometers lays within ±13’000 μm/m. This issue leads to an abrupt error as soon as the steel reaches its yield point. The fast nature of this process makes it impossible – even at very slow loading rates – to take new key measurements and thereby reset the maximum possible measurement range. In contrast, for materials without strain localisation (e.g. hot-rolled, stretched steels) it is possible to measure up to the rupture strain of the glass fibre itself at around 40’000 μm/m.

For rigidly bonded fibres without coating, the strain behaviour of the instrumented material can directly be measured and converted to stresses by applying the constitutive law of the material, as illustrated in Figure 1. Additional transformations (as e.g. conversion from engineering to true stress) proposed by other authors [37] are not required. This measurement procedure was successfully applied for the instrumentation of reinforcing bars in experimental campaigns at ETH Zurich [38–41], and its application to structural concrete panels will be shown in Section 4. These applications show that Rayleigh-based fibre optical strain sensing is very promising for structural concrete applications, given its capability to measure strains quasi-continuously. When used to instrument reinforcing bars, this technology provides very detailed information of processes inside the structures, which allow researchers having a much better insight into complex structural phenomena (e.g. bond) that were only investigated so far based on averaged, indirect or discrete information. However, there are some key aspects to be considered when using fibre optical strain sensing for structural concrete applications:

- The selection of the appropriate fibre type for a specific application is essential to obtaining reliable results, as will be shown in the experimental tests in Section 3.2.
- The fibres are delicate to handle and can break easily during fibre installation or specimen casting. Section 4.1 shows a protection system of the fibres that has proven to keep the probability of fibre damage during fabrication and installation of the specimens low.
- Determining the uncertainty of the measurements is difficult. To the authors’ knowledge, there are no studies addressing the accuracy of fibre optical sensors’ results in structural concrete applications. A first attempt in this direction is presented in Section 3.2, where the influence of some aspects is analysed and some measures are proposed.
- As for digital image correlation, the large amount of produced data requires developing specific processing tools to extract condensed, unbiased and useful information in an efficient way. Such tools have been implemented and have been used by the authors to e.g. compute local bond from fibre optical strain sensing results [39,40].

All fibre optic measurements described in this publication were conducted with the reflectometer ODiSI-A from LUNA Inc., allowing to measure up to 13'000 µm/m over a sensing length of 50 meters with a maximum sampling frequency of 1/3 Hz. Gauge length and sensor spacing were set to 5 mm.

3 Measurement uncertainty

In order to collect and evaluate reliable data in structural experiments, it is of utmost importance to assess the uncertainty of the novel optical measurements presented in Section 2. Assessing the uncertainty of a measurement comprises the quantitative estimation of the accuracy, i.e. assessing the deviation of the measured value to the true value. Such deviation from the true value is caused by a combination of systematic errors (bias) and random errors (noise). As it is impossible to measure all sources of errors, the assessment of the uncertainty will yield always a partial estimation of the real measurement accuracy. In the following some tests to estimate the uncertainty of DIC and distributed fibre optical measurements are proposed and the results are discussed.

3.1 Digital image correlation instrumentation

3.1.1 Sources of error

The following sections present an experimental methodology to estimate the uncertainty of DIC measurements. The uncertainty should be assessed for each test due to its dependency on a high number of test dependent parameters (quality of the calibration, environmental conditions, etc.). In addition to the quantification, this section discusses the main sources of errors in DIC measurements. This gives hints about the critical aspects to be considered when designing large scale structural tests in order to improve the accuracy of the measurements.

The error of DIC measurements can be split in the error when tracking the displacements between acquired images (image matching algorithm errors) and the errors when transforming the image displacements into real displacements of the tested element (errors of the optical system model). The influences on the matching algorithm accuracy have been studied extensively (e.g. in [20]) and are out of the scope of this paper. It depends on the phase accuracy of the interpolation filter used to reconstruct grey values at non-integer locations (required to get sub-pixel information) and on the image quality (contrast, size of the speckles, lighting conditions, etc.). The image quality is a key aspect to be considered, as it is responsible for most of the measurement noise (practical speckle and lighting recommendations to minimise the noise can be found elsewhere [20]). However, the bias induced by image matching algorithms is very low when modern algorithms implementing high order interpolation filters are used (e.g. the optimised 8th order coefficient filter used in this study exhibits a bias below 1/200 px even for very poor speckle quality). Therefore, most of the measurement bias is related to imperfections in the optical system model (insufficiently accurate calibration, errors due to out-of-plane motion, ambient conditions with changing temperature or air flow causing Schlieren effect, etc.). These aspects are critical for the final measurement accuracy in large scale structural tests, as the measurement bias can be easily one order of magnitude larger than the measurement noise, except for a very careful calibration (as will be shown in Section 3.1.3). It should be noted that the bias is similar between nearby points and tends to cancel out in results for relative displacements (used e.g. for computing crack kinematics). In addition to the bias measured in the following sections using 3D-DIC measurements, the error due to out-of-plane motion can be very relevant for the case of 2D-DIC measurements [20,42] unless telecentric lenses are used. 2D-DIC measurements, usually omitting a proper system calibration (i.e. determining the scale factor to convert pixels to millimetres in a simplified way), are very frequent in civil engineering experiments but unfortunately prone to very significant bias.

3.1.2 Proposed quantification methodology

For the assessment of the DIC measurement uncertainty, the procedures according to Table 1, which are based on the guidelines from the Association of German Engineers (Verein Deutscher Ingenieure, VDI 2626 [43]), are carried out. The Zero Displacement Test (ZDT) and the Zero Strain Test (ZST) characterise the ability of the measurement system to reproduce the assessed displacements and deformations whereas the Known Displacement Test (KDT) and the Known Strain Test (KST) indicate the ability of measuring absolute displacements and strains. The ZDT allows to assess the general noise floor of the measurement. Therefore, it can serve as an indicator for the choice of the ideal post-processing parameters – namely subset, step and filter size, which significantly influence the quality of the results from the correlation algorithm. A series of pictures – usually between 50 and 100 – without any movement nor deformation is taken in the ZDT, where every “measured” displacement or strain value signifies an error. In the Zero Strain Test, the specimen itself or a stiff plate with a speckle pattern is moved without applying any deformation (rigid body motion); multiple pictures are taken during the movement. The choice of a similar velocity and measurement frequency like in the real experiment is recommended. After removing the rigid body motion, the remaining “measured” values correspond to errors. For both ZDT and ZST, the area of interest should be divided into multiple sub-areas. In this study, an orthogonal grid of 10 x 10 rectangles was used. Within a sub-area, the mean and the standard deviation of the measurement points are obtained.

In the KDT, the specimen – after taking a reference measurement in its initial position – is moved along a known distance within the field of view. In this study, this was achieved by means of two steel blocks and one ceramic gauge block with a certified length according to DIN EN ISO 3650 [44] (see Table 1). The reference image is taken with the two steel blocks stacked on each other. Then, the ceramic block was placed between the steel blocks to move them exactly by a known length. This measurement should be carried out in the centre as well as on the edges of the field of view in order to assess properly the bias, which might be considerable larger near the edges of the field of view. The KST uses precisely certified templates of digitally deformed patterns that are printed on a flat plate (see Table 1). The plate is moved along different positions within the field of view.

3.1.3 Example of application

Test setup

The DIC setup in this example was the same as the one used in the Large Universal Shell Element Tester LUSET at ETH Zurich [45], see Figure 2. The 3D-DIC system was composed by two Allied Vision Prosilica GT6600 monochrome cameras (28.8 Megapixel, 36×24 mm sensor), positioned at a distance of 4000 mm to the specimen's surface. The baseline of 1230 mm between the two cameras resulted in a stereo angle of 17°, which is rather low (suggested ideal stereo angle is 20°-30° [21]) due to the geometric constraints of the testing facility [45]. Lenses with a focal length of 50 mm (Zeiss Planar T 1.4/50 mm) were used, which allowed a field of view of 2000×2800 mm at an average scale of 0.38 mm/pixel. For the ZDT and ZST a speckle pattern of randomly distributed black circular dots with a diameter of around 2 mm – which corresponds to approximately 5 pixels – was applied onto a base layer of white paint on the surface of a concrete panel to guarantee good contrast. The patterns for the KDT and KST were printed and glued on the blocks and a plate respectively. The correlation was carried out with the commercial software VIC-3D (Correlated solutions Inc. [46]).

The maximum displacement of the concrete panel in the ZST was 4% of the field of view and was applied by the LUSET testing facility [45] without generating significant forces on the specimen. The gauge blocks used in the KDT were certified in a calibration laboratory (deviation from the nominal length of 100 mm of 0.03 μm). The certification plate for the KST and the corresponding certified deformations were provided by isi-sys GmbH.

Results

The results from the ZDT serve as reference for the choice of the post-processing parameters. Figure 3 (a) shows the standard deviation of the individual sub-areas for various subset sizes as a function of their distance to the centre of the field of view. It can be clearly seen that the choice of the subset size has a significant influence on the noise level of the measurement. Moreover, the noise increases towards the edges of the area of interest which is most probably caused by the higher contrast of the pictures in the middle due to better lighting conditions and the lower performance of the lenses at the edges. Figure 3 (b) shows the standard deviation with respect to the subset size for one sub-area in the centre, one in the corner and the mean of all sub-areas. Based on a rule of thumb by Reu [21], the step size should lie between 1/3 and 1/2 of the subset size to prevent too much overlapping of the subsets. However, for the Automated Crack Detection and Measurement technique (Section 4.2), a denser displacement and strain field is preferred. Therefore, a step size of approximately 1/4 of the respective subset size was chosen.

There is an initially steep decrease in the noise level leading to an asymptote with increasing subset size, with hardly any difference between displacements *U* and *V* (in *x* and *y* direction, respectively). Figure 3 (b) allows the choice of an optimal subset size, which is a compromise between noise level and resolution of the data points. For all further analyses in this section, a subset size of 15 pixels at a step size of 4 was chosen. The standard deviation within a sub-area lies at around 0.5/100 of a pixel on average, and even for the worst values in the corner does not exceed 1/100 pixel.

For the chosen configuration, the strains were computed with various filter sizes, which signify the number of points over which the strains are derived from the displacement field. The principal strains for sub-areas in the centre and in the corner as well as the average over all sub-areas are plotted against the filter size in Figure 3 (c). Again, the choice of the filter size is a compromise between noise and spatial resolution of the strain field. For all further analyses, a filter size of 15 was chosen, which corresponds to a gauge length of 23 mm. The noise level of the strains lies at around 40 μm/m on average at a maximum in the corner of around 50 μm/m. Generally, the strains show much smaller differences in uncertainty between centre and corner than the displacements.

In the Zero Strain Test, the bias of the measurement with increasing displacement can be analysed in addition to the noise. The importance of a proper calibration is crucial for the resulting bias as can be shown in Figure 3 (d). The standard deviation of the remaining displacement *U* in *x* direction after the rigid body motion removal is plotted against the actual total displacement for each individual sub-area. Despite being a noise estimator not quantifying the total uncertainty, the standard deviation allows comparing different calibrations since it is sensitive to differential bias within each sub-area. Three different calibrations are examined in Figure 3 (d): (i) “random”, where only four randomly chosen calibration pictures are taken into account for the calibration; (ii) “all”, which uses a total of 50 calibration pictures covering all possible positions and rotations of the calibration plate with a rigid regular point grid; and (iii) “hybrid”, in which the standard calibration “all” is refined with the information from speckle images with a moving specimen [22]. Moreover, series “hybrid + filter” presents the results of the hybrid calibration refined by applying a time filter (a median filter with a size of 5 was chosen). At zero displacement, all calibrations display a standard deviation at a similar level, i.e. the noise of the measurement is independent of the calibration. However, this drastically changes with increasing movement of the specimen. The random calibration shows a large increase of the error (i.e. bias increases a lot with the applied movement). The normal calibration shows generally the same tendency but with lower bias. The hybrid calibration can mitigate the increasing bias with the displacement, as the noise level stays constant with increasing movement. The median filter reduces very significantly the noise level. Therefore, the hybrid calibration with median time filter size of 5 was used for the other uncertainty analyses in this study (except were mentioned specifically).

The uncertainty and its spatial distribution were quantified by the following spatial standard deviation parameters proposed by the VDI guidelines [43] for displacements (*NV*) and strains (*ND*), obtained from the ZST:

$$NV = \sqrt{\frac{1}{N}\sum_{q=1}^{N}\left(dx_q^2 + dy_q^2\right)}$$
$$ND = \sqrt{\frac{1}{N}\sum_{q=1}^{N}\left(\varepsilon_1^2 + \varepsilon_2^2\right)_q} \quad (1)$$

where dx_q and dy_q denote the measured displacements after rigid body removal of each point within the examined sub-area (*U* and *V* in VIC-3D) whereas ε_1 and ε_2 are the principal strains calculated from ε_{xx}, ε_{yy} and ε_{xy}. N is the number of measurement points within the sub-area.

In Figure 3 (e) and (f), the standard uncertainty values for displacement and strain are plotted in a pixel plot representing the sub-areas. The graph shows the state at maximum displacement in Figure 3 (d). One can see that most of the area of interest displays rather low uncertainty for the applied displacement (below 8 μm – i.e. 1/50 of a pixel – and 175 μm/m, respectively, for displacements and strains) and only the corner areas exhibit higher values. Since the specimen is moving to the left, the higher uncertainty at the left edge may be attributed to the worse lighting conditions. In the appendix, the reader may find more pixel plots of the standard uncertainty at different stages of the movement and for the different calibrations used. It should be noted that unless a very careful calibration is carried out, the uncertainty at the corner of the specimens is easily an order of magnitude higher than the values provided by DIC software manufacturers.

Table 2 shows the measurements from the KDT. For this analysis, a standard calibration was used. The measured distances between initial and final state of the steel blocks were averaged over five measurements in each of the four measured positions. The results were very accurate and insensitive to the measurement position. The absolute error is in the order of 10 μm (1/50 of a pixel), in line with the observations for the ZDT shown in Figure 3. This allows concluding that there was no significant bias due to any uncorrected scale factor (i.e. the reference length in the used calibration length was accurate).

Table 3 gives an overview of the measured strains obtained from the KST applied at nine different positions. For each position three different strain measurements – 5%, 10% and 20% – are carried out. There seems to be no influence regarding the position of the measurement, the direction of the strain nor the magnitude. The mean of the absolute error over all measurements lies around 80 μm/m, which corresponds well with the findings from the ZDT and ZST, showing that no bias results by large strains. One should note that the imposed strains are much higher than what would be expected in a usual concrete test specimen (ultimate compressive strain around -3‰) and hence, accurate strain measurements are expected in structural concrete experiments.

3.2 Distributed fibre optical strain sensing

3.2.1 Sources of error

The following sections present the results of several experiments that allow investigating the influence of various parameters on the uncertainty (mainly noise) of distributed fibre optical strain measurements. It should be noted that quantifying the uncertainty of fibre optical strain measurements is challenging due to the difficulty of having a reference measurement that is accurate enough to be considered representative of the true measurement value (most strain measurements are less accurate than fibre optics). Besides the discussion on quantification, the potential sources of error in fibre optical measurements are introduced thereafter.

The strain value in fibre optical measurements is normally calculated assuming a direct proportionality between the measured frequency shift and the strain. Every fibre type has its specific conversion factor, and it is therefore recommended to determine it for every fibre type individually by subjecting a fibre sample to a set of known uniform displacements [47,48]. Still, a bias will occur if the real physical relation deviates from the assumed proportionality. Such deviations are mainly caused by variations in temperature (ambient or of the measuring system, see Section 3.2.2) and to a lesser extent by variations in pressure, humidity, electromagnetic fields, etc. [49]. The bias resulting from temperature changes can be calculated and eliminated by using an unloaded fibre as reference.

Similar to the bias, the noise floor of fibre optical measurements depends on the ambient and spectrometer's temperature, the fibre type, the sensing fibre's length, its curvature relative to the reference state, the sensor quality (signal loss at splices, unwanted reflections at the end of the sensor, etc.), the key measurement (the zero measurement before the test, where the backscatter of the fibre in the unloaded stage is analysed), etc. It is hardly possible to quantify the noise floor for the entire duration of an experiment, as it is additionally highly dependent on the absolute strain level (see Section 3.2.3).

3.2.2 Influence of ambient conditions

To analyse the influence of the ambient conditions on noise and bias, the strains in a stationary fibre (12.54 m long, produced by Huber & Suhner AG, Switzerland) were measured over time. After taking a baseline, strains were measured for 9 hours and then the reflectometer was switched off. About 24 hours after the first measurement, the device was reconnected, the laser was aligned and strains were measured using the same baseline as the day before. Temperature in the room was recorded continuously during the test and the strains due to temperature variations (ε_T) were calculated considering the fibre's thermal expansion coefficient provided by the manufacturer of the reflectometer [50]. Figure 4 (a) shows the histograms of all 2508 measurement points in the fibre for three measurements taken at different times (0, 9 and 24 hours). A normal distribution was fitted to each histogram. The mean value μ shifted +12 µm/m and –11 µm/m at 9 and 24 hours respectively. This shift could be caused by strains due to changes in the ambient temperature and/or by other measurement bias. The calculation of the theoretically induced strains due to temperature during the first 9 hours of the measurement (Figure 4 (b)) gives about 60% of the total measured strains. Hence, the remaining difference indicates the existence of a small bias, which might be attributed to the heating up of the measuring device or to an inaccurate strain conversion factor (see Section 3.2.1). The noise, characterised by the standard deviation σ, increased from 1 to 10 µm/m in the first 9 measuring hours, but dropped to 5 µm/m after reconnecting the reflectometer (at 24 h). This shows that changes in the reflectometer's temperature might lead to small misalignments of the built-in laser components and increase the noise level. In any case, the quantified noise floor and bias are very low considering the requirements for most structural applications.

3.2.3 Influence of fibre type and strain level

The influence of various fibre coatings, various types of adhesive and various strain levels on the exhibited noise is examined by means of two direct tension tests on steel plates with variable cross section (see Figure 5 (a)). Both specimens were cut from a 6 mm thick cold-formed steel plate and had three sections with lengths of approximately 120 mm each and different widths of 30, 37.5 and 50 mm. Four fibres with properties according to Table 4 were glued on both sides of the specimens. Fibre FP1 was tested twice to evaluate repeatability. The fibres were glued with two adhesives with different stiffness to evaluate their ability to properly transfer shear without significant slip. An epoxy resin with low viscosity (Sikadur-52, Young's Modulus 1.8 GPa [51]), well suited for filling small notches containing a fibre, was used in specimen E. In specimen L, a two-phase adhesive with high viscosity (Loctite HY 4090, Young's modulus 0.57 GPa [52]), suitable for gluing a fibre directly onto the material, was used. All the fibres were spliced together to obtain one single measuring fibre. The noise floor at the beginning of the test was ±10 µm/m. For each section, two speckled areas in a distance of approximately 60 mm were applied and DIC measurements were taken as a reference. The specimens were loaded in uniaxial tension in five steps (4, 15, 30, 45 and 72 kN). The load was kept constant at every load level for at least 30 seconds.

Figure 5 (b) and (c) show the fibre optical strain measurements along specimens E and L at maximum load, where strains at every sensor point are averaged over the time interval with constant load. Horizontal lines indicate mean DIC strains between the two speckled areas on each section. Fibre strains measured on the same side as DIC strains (front side) are plotted in colour, while strains at the back side are plotted in grey. The mean values of all sensor points within a section of constant cross section are reported in Table 5, together with the theoretical strain value ($\varepsilon_{th}=F/(EA)$) calculated based on the applied load (F) and a nominal linear elastic stiffness (nominal cross section A, and elastic modulus assumed to be 210 GPa).

Mean fibre optical strains at the front side are in very good agreement with DIC results, regardless of fibre type and adhesive (deviations in the order of 50 µm/m, see Table 5). This confirms the results of similar experiments conducted at TU Munich [53]. Comparing the strain distribution in each section (Figure 5(b) and (c)), the measurement repeatability is excellent (the results of the two identical fibres FP1a and FP1b are almost identical) and no significant influences are observed regarding the used adhesive. Despite the more than three times different Young's modulus, which can serve as an estimate for the shear stiffness, both epoxy resin and two-phase adhesive ensure a proper shear transfer between coating and metal. However, the results are highly dependent on the fibre coating type. The acrylate-coated fibre (FA, blue line) exhibits non-constant strains over the areas with equal cross section, whereas polyimide-coated fibres (FP1a, FP1b and FP2, red lines) show constant strains, as would be expected. Additionally, the strain gradients at both ends of the glued part of the fibres are much higher for fibres with polyimide coating. As already stated by Quiertant et al. [32], these effects are due to the different characteristics of the coatings. Whereas acrylate is just covering the fibre and can easily be removed mechanically, polyimide forms a chemical bond to the glass of the cladding, which enhances the shear transfer between cladding, coating and adhesive. Therefore, in spite of being more difficult to handle (e.g. fibre stripping for splicing), polyimide-coated fibres should be used in tests where high strain gradients are expected (e.g. reinforcing bars in RC specimen between cracks).

When comparing the fibre optical strain measurements of the front and back sides, significant differences are observed. This can be attributed to the presence of bending actions, which are related to the slightly curved initial longitudinal geometry of the steel plates and to small misalignments of the applied tensile loads. Table 5 provides the mean between the front and back measurements, which represents the average tensile strain in the element. These values are systematically larger than the calculated theoretical strains (7% deviation on average). Given the good agreement with the DIC measurements on the front side, it is likely that this deviation is not due to a bias of the fibre optical measurement, but to an incorrect estimation of the elastic modulus used to calculate the theoretical strains. Therefore, the presented comparison with calculated theoretical strains is of great use as a plausibility check, but does not allow quantifying the measurement uncertainty.

The potential influence of the applied strain level on the measurement noise is studied in Figure 5 (d). This figure shows for the direct tension test L the evolution over time of the mean strains and the standard deviation of all sensor points within the 50 mm wide section on the front side. Only the results of fibres FA and FP1b and the results of the DIC measurements are represented. The mean fibre optical strains (black lines) show the load path with the distinct plateaus when the load was held constant, and are in good agreement with the strains from the DIC measurements. The standard deviation (red lines on the right axis) gives an estimate of the measurement noise, which is dependent on the strain level and on the fibre type. In the acrylate-coated fibre the noise floor is initially very small (σ = 4 µm/m), but it increases up to 42 µm/m at the maximum applied strain level (1329 µm/m). While the initial noise level in the polyimide-coated fibre is higher (σ = 7 µm/m), it shows a less pronounced strain level dependency, what leads to a noise of only 20 µm/m at the maximum strain level.

3.2.4 Influence of secondary actions and reinforcing bar geometry

Instrumenting reinforcing bars in structural concrete experiments with several sensing fibres per bar allows capturing very detailed local phenomena that could not be measured so far with conventional instrumentation. Examples of these local phenomena are given in Figure 6, where the measured strains in a reinforcing bar of a standard pull-out test [54] are shown. The pull-out test was conducted with a reinforcing bar of 26 mm diameter and steel B700B (nominal yield strength of 700 MPa), which was embedded in a concrete (f_c = 38 MPa) block of 400x400x965 mm. Each bar was instrumented with two polyimide-coated sensing fibres glued into grooves of 1x1 mm size (one was placed along the ridge of the bar, whereas the other crossed its ribs, see Figure 6). As discussed in Section 3.2.3, the divergence in the strains between both fibres denotes (and allows quantifying) the presence of significant bending actions, which are typical in such tests due to slight misalignments of the loading apparatus. The mean value of both measured strains gives an estimation of the applied average tensile strains. When examining the shape of both fibre strain curves, significant differences are observed. The strain curve of the fibre FO1 along the reinforcing bar's ridge shows very smooth results, while in the curve of the fibre FO2 crossing the ribs local peaks in a regular distance are observed. The distances of these peaks match very well the rib spacing (10-12 mm), which indicates that the ribs have an influence on the local strain behaviour of the reinforcing bar. Although the strain variation of the fibres crossing the ribs does not change the overall interpretation of the test result and could even be filtered out, it should not be treated as noise.

4 Application to concrete panels

This section presents and discusses the results of a series of two concrete panel tests subjected to diagonal tension, which were conducted to evaluate the potential and the concept of the combined application of fibre optical strain sensing on the reinforcing bars and digital image correlation on the concrete surface. These tests were used to inform the instrumentation setup to be used in the Large Universal Shell Element Tester LUSET at ETH Zurich [45] consisting in 2 m side length and 350 mm thickness panels. Hence, in spite that the size of the concrete panels is smaller than the panels in the LUSET, the instrumentation was set as in the latter.

4.1 Description of the experimental program

The panels of 600 mm side length and 125 mm thickness were reinforced with orthogonal stirrups of diameter 10 mm parallel to the x-direction and either stirrups of diameter 6 mm (specimen FODIC-10-6) or 8 mm (specimen

FODIC-10-8) in the *y*-direction as can be seen in Figure 7 (a). Two 22 mm headed bars were placed over one diagonal for the load introduction. The stirrups consisted of hot-rolled, cold-stretched steel, lacking a distinct yield plateau. The mechanical properties were obtained from standard tensile tests and are given in Table 6. The concrete had a maximum aggregate size of 16 mm and a nominal characteristic compressive cylinder strength of 40 MPa. Diagonal tension was applied by pulling the diagonal bars in a universal testing machine (as shown in Figure 7 (a)). The load case is not of particular interest for the structural behaviour, but is a good benchmark for the instrumentation as it generates a complex crack pattern. A loading rate of 0.06 mm/min was initially applied, which was increased in the post-peak phase. With the stirrups oriented at 45° to the direction of the applied force, a combined loading in shear and biaxial tension was obtained with respect to the reinforcement directions.

Both stirrup legs were instrumented with glass fibres, which were glued with epoxy resin in 1x1 mm grooves carved along the length of the bars (Figure 7 (b)). As reported in [32], this installation procedure minimises the impact on bond behaviour, maximises the protection of the fibres inside the specimen and ensures a proper shear transfer between rebar and adhesive. Acrylate-coated fibres were used as the better performance of the polyimide-coated fibres (discussed in Section 3.2.3) was yet unknown when conducting these experiments. Fibre ends were put into small rubber tubes to lead them out of the specimen and protect them during casting. In the transition zone between glued and unglued sections, fibres were additionally protected by hot glue. This protection concept worked very well, as only 8% of the fibres were damaged during production and hence unable to transmit the laser signal. The end of the fibres was cut manually at ~45° and placed into water or epoxy resin. This is a simple solution to produce a fibre termination that ensures a proper signal loss and reliably avoids mirroring effects due to reflections. The noise floor at the beginning of the test was within ±20 μm/m and increased with higher strain level (see Section 3.2.3). Engineering stresses and forces were calculated using the stress-strain-relationship of every rebar type obtained from the steel tensile tests and considering the nominal cross sectional area.

The same DIC setup as reported in Section 3.1.3 was used, but lenses of 28 mm focal length (Zeiss Distagon-2/28 mm) were installed in this case. This led to the cameras being positioned at a distance of 2400 mm to the specimen's surface. The baseline between the two cameras was kept as in Section 3.1.3 which resulted in a stereo angle of 28°. The used speckle pattern is shown in Figure 7 (c), together with the main parameters used in the DIC post-processing. A standard calibration was used in this case. The measurement uncertainty calculated following the procedure presented in Section 3.1 resulted in a standard deviation of the uncertainties in strains of 250 μm/m and of 0.01 mm in displacements, both for the maximum displacement applied in the test. These values are larger than the ones observed in Section 3.1.3, which can be explained due to the use of a lens with a large focal lens (with larger distortions) and to not yet using a more refined hybrid calibration.

4.2 Automated crack detection and measurement

The limitations and bias introduced when only selected points of selected cracks are measured (either by eye inspection or by manual post-processing of DIC measurements) can be overcome by developing a suitable crack processing algorithm based on DIC measurements, as e.g. the open-source ACDM (Automated Crack Detection and Measurement) software developed by the authors [25] and available at: https://gitlab.ethz.ch/ibk-kfm-public/acdm. The main steps of ACDM are graphically outlined in Figure 1. The detection concept follows the idea that the crack pattern as discrete crack lines is obtained by tracking Canny edges [55] in the principal tensile strain field obtained from the DIC measurements. In order to obtain the crack kinematics of a certain point of the crack line, the relative movement of both crack lips is determined using the DIC displacement field following a similar approach as proposed by Campana et al. [19]. ACDM allows measuring crack opening and crack sliding quasi continuously (over time and over the length of every single crack) with little human effort, which makes it particularly suitable to large scale experiments with complex crack patterns (as e.g. those performed in the Large Universal Shell Element Tester LUSET [45] for which ACDM was originally developed). The ACDM software was used to compute all crack patterns and cracks kinematics in Figure 8 and Figure 9.

4.3 Results and discussion

Figure 8 shows the combined results of DIC and fibre optics for both specimens and two different load steps. The cracks are shown as black lines with the line thickness indicating their opening. The colours along the stirrups indicate the stresses calculated for the front layer and the line thickness corresponds to the sum of forces for both stirrup legs. Since the optical fibres left the specimen at the boundary area, the DIC field of view and the tracked cracks do not reach the specimen's edge. In specimen FODIC-10-6 the stirrups of diameter 10 mm remained elastic during the entire test whereas the stirrups of diameter 6 mm reached the yield point at approximately 110 kN. In specimen FODIC-10-8 at a load level of 150 kN, the stresses in most of the stirrups are close to yielding. The location of larger cracks can clearly be identified in the fibre optical measurements, and match very accurately the crack location detected by the ACDM based on the DIC measurement. It should be noted that, as discussed in Section 3.2.3, the acrylate coating of the fibres impedes a proper shear transfer between coating and cladding. Therefore, the magnitude of the measured strains in zones of high strain gradients might deviate from the true value.

Reinforcement strains of both legs of stirrup A (Ø10, y = -50 mm) of specimen FODIC 10-8 (see Figure 8 (d) for exact location) are shown in Figure 9 (a) for different load steps together with the measured openings and inclinations of the cracks crossing the stirrup. Cracks 1 and 2 close to the edge of the specimen are occurring at 90 kN, whereas crack 3 is formed at a load of approximately 120 kN. As observed in Figure 8, the location of the cracks can be detected independently with both optical systems and the positions match accurately. The fibre optical strains of the front and back legs of the stirrup are very similar. Again, measured strains can deviate from the actual strains due to the acrylate coating of the fibres. This effect can be observed for the region around crack 1, where much higher strains in the reinforcement would have been expected to be consistent with the existing large opening of crack 1.

Figure 9 (b) shows the continuous evolution with the applied force of the opening of crack 3 and the steel strains for both stirrup legs at this position. The sudden formation of the crack at 120 kN leads to a significant drop in the load. A jump in the steel strains and in the crack opening of about 1‰ and 0.2 mm respectively was tracked successfully in this fast process, demonstrating the capability of optical measurements to monitor the cracking phase of concrete structures.

A combination of both measuring techniques, as shown in the Figure 8 and Figure 9, allows to (i) mutually verify their results, (ii) link the reinforcing bars' stress distribution to the concrete kinematics, and by this (iii) investigate the load distribution in the different element parts over time on a very intuitive basis. This contributes to a better understanding of processes like crack formation and crack kinematics. As a possible further step, equilibrium along a crack can be analysed, by assuming that stirrups only transfer forces in their direction (e.g. neglecting dowelling action). Considering the applied external forces, the contribution of e.g. aggregate interlock could be estimated. An evaluation of the strain distributions along a reinforcing bar at different load states, similar to the one suggested in Figure 9, rises the opportunity to further investigate bond between reinforcement and concrete, which has a direct link to fundamental aspects of structural concrete as the serviceability behaviour and deformation capacity.

5 Concluding remarks

This publication shows that the combined application of distributed fibre optical and digital image correlation measurements has a great potential to increase knowledge in many fields of structural concrete, such as bond and cracking behaviour or load carrying and deformation capacity of elements with low amounts of transverse reinforcement. Both measuring systems can document the phenomenological effects continuously, comprehensively and at a very detailed level, both inside and on the surface of the analysed structure, without affecting the mechanical behaviour - a radical progress compared to conventional instrumentation. This promises a better understanding of the underlying mechanisms and the development of sound mechanical models for existing structures and non-conventional materials, which is essential to avoid unnecessary retrofitting measures and to open the way for the design of leaner new structures. However, there are some key aspects herein discussed that should be considered when using these instrumentations in order to guarantee the measurements to be reliable and therefore suitable not only for qualitative, but also for quantitative analysis.

Digital image correlation allows tracking the displacements of an entire surface, but the uncertainty of the measurements is highly dependent on the test conditions and user care, particularly regarding calibration. In this publication, various complementary methods suitable for large-scale structural experiments were introduced aiming at investigating the uncertainty of digital image correlation-based measurement systems. The measurement uncertainty provided by the manufacturers of DIC-systems (i.e. around 1/100 of a pixel) is obtained only in very controlled laboratory conditions and often merely refers to the uncertainty of the correlation algorithm. Thus, it is not representative for the application on large-scale structural elements in which uncertainties an order of magnitude higher might be easily obtained. Therefore, the assessment of uncertainty for each test, considering the influences of the calibration and the environment – such as the lighting conditions or the speckle quality – is crucial for the proper evaluation of the experimental data. The presented Zero Displacement and Zero Strain Tests are easy to prepare and conduct. They allow quantifying noise and bias and choosing the optimum post-processing parameters depending on the actual purpose of the analysis. Image quality (contrast, size of the speckles, etc.) was detected as one of the most influencing parameters for the quality of the correlation, which is responsible for most of the measurement noise. However, the finally achieved uncertainty is highly dependent on the quality of the calibration. The best results can be obtained when a hybrid calibration is performed, combining the information from a standard calibration and moving speckle images. An additional source of bias in digital image correlation structural measurements might be introduced in the post-processing phase if only selected information of the large amount of produced data is used (e.g. few virtual strain gauges). This can be overcome by using tools such as the presented Automated Crack Detection and Measurement software that allows measuring crack opening and crack sliding quasi continuously, requiring little human effort.

Distributed fibre optical strain sensing allows measuring strains quasi-continuously with a very high precision without biasing the specimen's behaviour. By gluing the fibres onto the reinforcing bars, continuous measurements inside the specimens are obtained, providing direct insight into the mechanisms of RC structures. However, with the higher level of detail, other phenomena become visible (as e.g. the influence of a complex stress state directly at the ribs of a reinforcing bar), which may not be of main interest but complicate the evaluation. There exist various sources of errors in fibre optical strain sensing: Temperature variations (ambient or heating-up of the measuring device) and deviations of the strain conversion factor from the assumed value can cause a bias, whereas the noise level is influenced by temperature, sensor length, sensor quality, and strain level. The uncertainty quantification for fibre optical strain measurements is challenging and limited to basic assessments such as the evaluation of the noise floor in the unloaded state and the comparison with values from strain gauges or DIC. These comparisons are limited to the accuracy of the comparative measurements, which is usually worse than fibre optics. The conducted tests show that the coating material of the fibre has a major influence on the strain data quality: a rigid coating (as polyimide) ensures a proper shear transfer between adhesive and cladding, whereas a mechanically weak coating (as acrylate) leads to local slip at high strain gradients. Hence, it is recommended using polyimide-coated fibres when instrumenting reinforcing bars in RC specimens, as they typically reach high strain gradients.

Acknowledgements

Part of the experiments described in Section 3.2 were carried out as a part of the Master's Project of Nathalie Reckinger and Caroline Wirion at ETH Zurich, whose contributions are greatly acknowledged. The authors would also like to thank the staff of the structural engineering laboratory at ETH Zurich for their support, Walter Kaufmann for the proofreading and the providers of the digital image correlation system Isi-sys GmbH and Correlated Solutions Inc. for their support and suggestions for the uncertainty quantification.

References

[1] Nielsen MP. Limit Analysis and Concrete Plasticity. Prentice-Hall Series in Civil Engineering. New Yersey: Englewood Cliffs; 1984.

[2] Thürlimann B, Marti P, Pralong J, Ritz P, Zimmerli B. Anwendung der Plastizitätstheorie auf Stahlbeton. Unterlagen zum Fortbildungskurs, Institut für Baustatik und Konstruktion, ETH Zürich; 1983.

[3] Wangler T, Roussel N, Bos FP, Salet TAM, Flatt RJ. Digital Concrete: A Review. Cement and Concrete Research 2019;123:105780. https://doi.org/10.1016/j.cemconres.2019.105780.

[4] Asprone D, Menna C, Bos FP, Salet TAM, Mata-Falcón J, Kaufmann W. Rethinking reinforcement for digital fabrication with concrete. Cement and Concrete Research 2018;112:111–21. https://doi.org/10.1016/j.cemconres.2018.05.020.

[5] Kaufmann W, Marti P. Structural Concrete: Cracked Membrane Model. Journal of Structural Engineering 1998;124:1467–75. https://doi.org/10.1061/(ASCE)0733-9445(1998)124:12(1467).

[6] Vecchio FJ, Collins MP. The Modified Compression Field Theory for Reinforced Concrete Elements Subjected to Shear. ACI Journal 1986;83:219–31.

[7] Kaufmann W, Mata-Falcón J, Amin A. Compression field analysis of FRC based on the cracked membrane model. ACI Structural Journal 2019;116:213–24. https://doi.org/10.14359/51716763.

[8] Markic T, Amin A, Kaufmann W, Pfyl T. Strength and deformation capacity of tension and flexural RC members containing steel fibres. ASCE Journal of Structural Engineering 2020;in print. https://doi.org/https://doi.org/10.1061/(ASCE)ST.1943-541X.0002614.

[9] Valeri P, Fernández Ruiz M, Muttoni A. New perspectives for design of lightweight structures by using textile reinforced concrete. Proceedings of the fib Symposium 2019, Kraków, Poland: Fédération Internationale du Béton (fib); 2019, p. 73–80.

[10] Kaufmann W, Mata-Falcón J, Beck A. Future directions for research on shear in structural concrete. fib Bulletin 85: Towards a rational understanding of shear in beams and slabs, 2018.

[11] Mata-Falcón J, Pallarés L, Miguel PF. Proposal and experimental validation of simplified strut-and-tie models on dapped-end beams. Engineering Structures 2019;183:594–609. https://doi.org/10.1016/j.engstruct.2019.01.010.

[12] Walraven JC, Reinhardt HW. Theory and Experiments on the Mechanical Behaviour of Cracks in Plain and Reinforced Concrete Subjected to Shear Loading. HERON 1981;26 (1A).

[13] Eligehausen R. Local bond stress-slip relationships of deformed bars under generalized excitations: experimental results and analytical model. Berkeley, California: Earthquake Engineering Research Center, College of Engineering, University of California; 1983.

[14] Alvarez M. Einfluss des Verbundverhaltens auf das Verformungsvermögen von Stahlbeton. vol. 236. Basel, Switzerland: Birkhäuser; 1998.

[15] Walraven JC. Fundamental Analysis of Aggregate Interlock. Journal of the Structural Division, ASCE 1981;107:2245–70.

[16] Beck A, Gehri N, Mata-Falcón J, Kaufmann W. Cracked Membrane Model with Fixed, Interlocked Cracks: Numerical Implementation and Validation. Journal of Structural Engineering, ASCE 2020;146. https://doi.org/https://doi.org/10.1061/(ASCE)ST.1943-541X.0002461.

[17] Bignell VF, Smalley V, Roberts NP. A new photoelastic material for use in problems concerning reinforced concrete. Magazine of Concrete Research 1963;15:171–6. https://doi.org/10.1680/macr.1963.15.45.171.

[18] Morice PB, Base GD. The design and use of a demountable mechanical strain gauge for concrete structures. Magazine of Concrete Research 1953;5:37–42. https://doi.org/10.1680/macr.1953.5.13.37.

[19] Campana S, Fernández Ruiz M, Anastasi A, Muttoni A. Analysis of shear-transfer actions on one-way RC members based on measured cracking pattern and failure kinematics. Magazine of Concrete Research 2013;65:386–404. https://doi.org/10.1680/macr.12.00142.

[20] Sutton MA, Orteu JJ, Schreier H. Image Correlation for Shape, Motion and Deformation Measurements: Basic Concepts, Theory and Applications. Springer US; 2009.

[21] Reu P. Introduction to Digital Image Correlation: Best Practices and Applications. Experimental Techniques 2012;36:3–4. https://doi.org/10.1111/j.1747-1567.2011.00798.x.

[22] Schreier HW. Accuracy Improvements and Meaningful Error Metrics for Stereo System Calibration. Extended Abstract, iDICs, Barcelona, Spain: 2017.

[23] Cavagnis F, Ruiz MF, Muttoni A. Shear failures in reinforced concrete members without transverse reinforcement: An analysis of the critical shear crack development on the basis of test results. Engineering Structures 2015;103:157–73.

[24] Huber P, Huber T, Kollegger J. Investigation of the shear behavior of RC beams on the basis of measured crack kinematics. Engineering Structures 2016;113:41–58. https://doi.org/https://doi.org/10.1016/j.engstruct.2016.01.025.

[25] Gehri N, Mata-Falcón J, Kaufmann W. Automated crack detection and measurement based on digital image correlation. Construction and Building Materials 2020;256:119383. https://doi.org/10.1016/j.conbuildmat.2020.119383.

[26] Henault J-M, Quiertant M, Delepine-Lesoille S, Salin J, Moreau G, Taillade F, et al. Quantitative strain measurement and crack detection in RC structures using a truly distributed fiber optic sensing system. Construction and Building Materials 2012;37:916–23. https://doi.org/10.1016/j.conbuildmat.2012.05.029.

[27] Samiec D. Verteilte faseroptische Temperatur- und Dehnungsmessung mit sehr hoher Ortsauflösung. Photonik 2011;6:4.

[28] Soller BJ, Gifford DK, Wolfe MS, Froggatt ME. High resolution optical frequency domain reflectometry for characterization of components and assemblies. Optics Express 2005;13:666–674.

[29] Hauswirth D. A study of the novel approaches to soil displacement monitoring using distributed fiber optic strain sensing. ETH Zurich, 2014.

[30] Kechavarzi C, Soga K, de Battista N, Pelecanos L, Elshafie M, Mair R. Distributed Fibre Optic Strain Sensing for Monitoring Civil Infrastructure. London: ICE Publishing; 2016.

[31] Billon A, Hénault J-M, Quiertant M, Taillade F, Khadour A, Martin R-P, et al. Qualification of a distributed optical fiber sensor bonded to the surface of a concrete structure: a methodology to obtain quantitative strain measurements. Smart Materials and Structures 2015;24:115001. https://doi.org/10.1088/0964-1726/24/11/115001.

[32] Quiertant M, Baby F, Khadour A, Marchand P, Rivillon P, Billo J, et al. Deformation monitoring of reinforcement bars with a distributed fiber optic sensor for the SHM of reinforced concrete structures, 2012.

[33] Her S-C, Huang C-Y. Effect of Coating on the Strain Transfer of Optical Fiber Sensors. Sensors 2011;11:6926–41. https://doi.org/10.3390/s110706926.

[34] Rocha M, Brühwiler E, Nussbaumer A. Geometrical and Material Characterization of Quenched and Self-Tempered Steel Reinforcement Bars. Journal of Materials in Civil Engineering 2016;28:04016012. https://doi.org/10.1061/(ASCE)MT.1943-5533.0001355.

[35] Russwurm D. Betonstähle für den Stahlbetonbau. Wiesbaden Und Berlin: Bauverlag; 1993.

[36] Haefliger S, Fomasi S, Kaufmann W. Influence of strain-rate and microstructure on the stress-strain characteristics of reinforcing steel. Submitted on 2019 for Publication Construction and Building Materials n.d.

[37] Malek A, Scott A, Pampanin S, Hoult NA. Postyield Bond Deterioration and Damage Assessment of RC Beams Using Distributed Fiber-Optic Strain Sensing System. Journal of Structural Engineering 2019;145:04019007. https://doi.org/10.1061/(ASCE)ST.1943-541X.0002286.

[38] Gomer A. Zugversuche an mit CFK-Lamellen verstärkten Stahlbetonelementen. Master's Thesis. Institut für Baustatik und Konstruktion, ETH Zürich, 2017.

[39] Galkovski, Tena. Bond behaviour of structural concrete. Master's Thesis. Institute of Structural Engineering, ETH Zurich, 2017.

[40] Wehrli S. Pull-out tests on reinforcing bars using distributed fibre optical strain measurement. Master's Thesis. Institute of Structural Engineering, ETH Zurich, 2018.

[41] Haefliger S, Mata-Falcón J, Kaufmann W. Application of distributed optical measurements to structural concrete experiments. SMAR 2017 Proceedings, ETH Zurich: 2017.

[42] Sutton MA, Jan JH, Tiwari V, Orteu JJ. The effect of out-of-plane motion on 2D and 3D digital image correlation measurements - ScienceDirect. Optics and Lasers in Engineering 2008;46:848. https://doi.org/https://doi.org/10.1016/j.optlaseng.2008.05.005.

[43] Fachbereich Prozessmesstechnik und Strukturanalyse. VDI/VDE 2626 Blatt 1 - Optische Messverfahren - Bildkorrelationsverfahren - Grundlagen und Begriffe. VDI/VDE-Gesellschaft Mess- und Automatisierungstechnik; 2018.

[44] DIN EN ISO 3650:1999-02, Geometrische Produktspezifikationen (GPS)_- Längennormale_- Parallelendmaße (ISO_3650:1998); Deutsche Fassung EN_ISO_3650:1998. Beuth Verlag GmbH; n.d. https://doi.org/10.31030/7453787.

[45] Kaufmann W, Beck A, Karagiannis D, Werne D. The Large Universal Shell Element Tester LUSET. Zurich: Institute of Structural Engineering, ETH Zurich; 2019.

[46] VIC-3D. Correlated Solutions Inc.; 2019.

[47] Woschitz H. Faseroptische Erweiterung des geodätischen Messlabors der TU Graz. Vgi 2013.

[48] Klug F, Lackner S, Lienhart W. Monitoring of railway deformations using distributed fiber optic sensors. Proceedings of the Joint International Symposium on Deformation Monitoring, Vienna, Austria, vol. 30, 2016.

[49] Kreger ST, Gifford DK, Froggatt ME, Soller BJ, Wolfe MS. High resolution distributed strain or temperature measurements in single-and multi-mode fiber using swept-wavelength interferometry. Optical Fiber Sensors, Optical Society of America; 2006, p. ThE42.

[50] LUNA Inc. Users Guide ODiSI-A Software 1.3 2013.

[51] Sika Schweiz AG. Sikadur-52 Injection - Product Data Sheet 2011.

[52] Henkel Europe. Loctite HY 4090 GY - Product Data Sheet 2017.

[53] Schmidt-Thrö G, Scheufler W, Fischer O. Kontinuierliche faseroptische Dehnungsmessung im Stahlbetonbau. Beton- Und Stahlbetonbau 2016;111:496–504. https://doi.org/10.1002/best.201600026.

[54] AC 308 IC. Acceptance Criteria for Post-Installed Adhesive Anchors in Concrete Elements 2009.

[55] Canny J. A Computational Approach to Edge Detection. IEEE Transactions on Pattern Analysis and Machine Intelligence 1986;PAMI-8:679–98. https://doi.org/10.1109/TPAMI.1986.4767851.

Appendix

This appendix presents additional analyses of the quantification of the uncertainty, which complement the information provided in Section 3.1.3. Figures A.1 and A.2 present the spatial standard deviation parameters for displacements (*NV*) and strains (*ND*) respectively. These plots are analogous to the ones shown in Figure 3 (e) and (f), but at different stages of the movement and for the different calibrations used.

In Figure A.1 the results of the displacement uncertainty without movement are very similar among all the calibrations. No significant bias with the applied displacement can be observed when a hybrid calibration is used. However, the bias is very significant and increases with the displacement when a conventional calibration is conducted, especially when only four calibration pictures are used ("random"). Where present, the bias of the displacement is larger in the corners of the field of view.

The uncertainty results for the full field strains (Figure A.2) do not show as clear tendencies as the displacements. The uncertainty increases slightly with the applied displacement, but no concluding tendency can be obtained among the different calibrations. This reveals that, despite that the displacement field has significant bias, this might not apply to the calculated local strains as the bias between close points tends to be the same. A slightly worse uncertainty is obtained in the corners of the field of view. A similar tendency as for the full field strains presumably applies to measurements such as crack kinematics, where relative distances between close points are calculated.

Table captions

Table 1. Proposed test methods for the uncertainty assessment of DIC measurements.

Table 2. Measured DIC displacements from Known Displacement Test.

Table 3. Measured DIC strains from Known Strain Test.

Table 4. Properties of fibres used in the direct tension tests.

Table 5. Strains measured in different sections of specimens in the direct tension tests L and E at F=72 kN; mean fibre optical strains within each section at front (ε_{FO}^{front}) and back side (ε_{FO}^{back}); average of front and back side fibre optical strains (ε_{FO}^{mean}); DIC strains at front side ($\varepsilon_{DIC}^{front}$); calculated theoretical strain assuming linear elastic behaviour (ε_{th}).

Table 6. Material properties of the reinforcement used in the panel tests FODIC-10-6 and FODIC-10-8.

Figure captions

Figure 1. Combined use of digital image correlation (DIC) and distributed fibre optical strain instrumentation (FO): (a) general setup of possible structural concrete experiment with speckled surface and reinforcing bars instrumented with optical fibres; (b) FO continuous strain measurement along one bar and calculation of stresses based on the stress-strain relationship obtained from standard material tensile tests; (c) speckle pattern, strain field obtained with DIC and crack pattern and kinematics computed automatically from the measured DIC strain and deformation fields.

Figure 2. Digital image correlation setup in the Large Universal Shell Element Tester used for the uncertainty quantification.

Figure 3. Results of the DIC uncertainty quantification: (a) standard deviation of the displacement in ZDT, dependent on the distance to the image centre; (b) standard deviation of the displacement in ZDT, dependant on the subset size; (c) standard deviation of the principal strains in ZDT, dependent on the filter size; (d) comparison of the measurement error in ZST for different calibrations; (e) benchmark value NV for the displacement measurements in ZST according to VDI 2626 [43]; (f) benchmark value ND for the strain measurements in ZST according to VDI 2626 [43].

Figure 4. Fibre optical strain measurements on a stationary fibre: (a) histograms and fitted normal distributions (red) of three measurements at different times; (b) evolution over time of mean ($\mu(\varepsilon_{FO})$) and standard deviation ($\sigma(\varepsilon_{FO})$) of strains along the entire fibre, together with the calculated strains due to temperature ($\varepsilon_T(\Delta T)$).

Figure 5. Fibre optical strain measurements on two direct tension tests. Fibres of various types were glued with two different adhesives: (a) geometry of specimens with fibre optical and DIC instrumentation; (b) measured fibre

optical and DIC strains over length for specimen with epoxy-glued fibres at 72 kN; (c) measured fibre optical and DIC strains over length for specimen with Loctite-glued fibres at 72 kN; (d) evolution over time of mean strains and standard deviation in the 50 mm wide section for specimen with Loctite-glued fibres, together with DIC strains.

Figure 6. Local phenomena in reinforcing bars observed with fibre optical strain sensors in a pull-out test. Left: measured strains and corresponding stresses of fibres FO1 and FO2 (black) placed opposite to each other, together with their mean value (red); right: geometry of the reinforcing bar with the installed fibres.

Figure 7. Setup of panel tests FODIC-10-6 and FODIC-10-8: (a) Geometry and reinforcement layout of the specimens (dimensions in [mm]); (b) optical fibre (yellow) in groove of stirrup Ø10 leaving the glued section and continuing in tube; (c) applied speckle on concrete surface for DIC measurements with main parameters of the correlation.

Figure 8. Combined results of fibre optical and DIC measurements: Crack locations and openings together with steel stresses in the front layer and stirrup forces for FODIC-10-6 at (a) 80 kN and (b) 110 kN; for FODIC-10-8 at (c) 90 kN and (d) 150 kN.

Figure 9. Results of steel strains and crossing cracks for stirrup A (Ø10, y = -50 mm) for FODIC-10-8: (a) measured strains for different load steps with position, orientation and opening of cracks; (b) continuous results over time for crack 3 (x = 20 mm).

Figure A.1. Results of the DIC uncertainty quantification: uncertainty value *NV* of the displacements in ZST according to VDI 2626 [43] for different calibrations and applied displacements.

Figure A.2. Results of the DIC uncertainty quantification: uncertainty value *ND* for the full field strain measurements in ZST according to VDI 2626 [43] for different calibrations and applied displacements.

Tables

Table 1. Proposed test methods for the uncertainty assessment of DIC measurements.

Proposed test methods		Applied displacement	Applied strain	Measured magnitudes	Estimated uncertainty
Zero Displacement Test (ZDT)	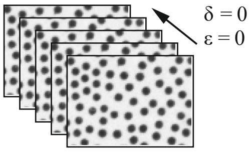	Zero	Zero	All	Noise floor
Zero Strain Test (ZST)	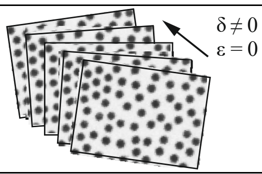	Unknown	Zero	All	Noise + bias (partially)
Known Displacement Test (KDT)	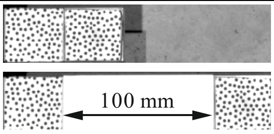	Known	Zero	Local displacement	Noise + bias
Known Strain Test (KST)	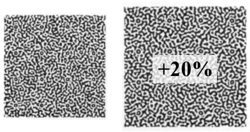	Unknown	Known	Local strain	Noise + bias

Table 2. Measured DIC displacements from Known Displacement Test.

Position	V_0 [mm]	V_1 [mm]	ΔL [mm]	abs. error [mm]
centre 1	0.0005	100.0072	100.0067	0.0067
centre 2	0.0010	100.0129	100.0119	0.0119
edge 1	0.0025	99.9962	99.9937	-0.0063
edge 2	-0.0015	100.0098	100.0114	0.0114

Table 3. Measured DIC strains from Known Strain Test.

Position	ε_{xx} [‰]	ε_{yy} [‰]	$\Delta\varepsilon_{xx}$ [µm/m]	$\Delta\varepsilon_{yy}$ [µm/m]	$\Delta\varepsilon_{xx}/\varepsilon_{xx}$ [‰]	$\Delta\varepsilon_{yy}/\varepsilon_{yy}$ [‰]
top-left	49.9840	50.0812	-56.0	71.2	-1.12	1.42
	99.9645	99.9538	-165.5	-86.2	-1.66	-0.86
	199.9480	199.8479	-202.0	-272.1	-1.01	-1.36
top-centre	49.9727	50.0721	-67.3	62.1	-1.35	1.24
	100.0727	100.0208	-57.3	-19.2	-0.57	-0.19
	200.1472	200.0805	-2.8	-39.5	-0.01	-0.20
top-right	50.0523	50.1748	12.3	164.8	0.25	3.29
	100.1252	100.1863	-4.8	146.3	-0.05	1.46
	200.2027	200.1340	52.7	14.0	0.26	0.07
centre-left	50.0342	50.0149	-5.8	4.9	-0.12	0.10
	100.1442	99.9901	14.2	-49.9	0.14	-0.50
	200.2502	200.0051	100.2	-114.9	0.50	-0.57
centre	50.0085	50.0655	-31.5	55.5	-0.63	1.11
	100.0424	100.0150	-87.6	-25.0	-0.88	-0.25
	200.1488	199.9850	-1.2	-135.0	-0.01	-0.68
centre-right	49.9852	49.9825	-54.8	-27.6	-1.10	-0.55
	100.0961	100.0069	-33.9	-33.1	-0.34	-0.33
	200.1562	200.0474	6.2	-72.6	0.03	-0.36
bottom-left	49.9874	49.9545	-52.6	-55.5	-1.05	-1.11
	100.0304	99.8849	-99.6	-155.1	-1.00	-1.55
	200.0746	200.0097	-75.4	-110.3	-0.38	-0.55
bottom-centre	49.9525	49.9235	-87.5	-86.5	-1.75	-1.73
	100.0588	100.1338	-71.2	93.8	-0.71	0.94
	200.2029	200.0703	52.9	-49.7	0.26	-0.25
bottom-right	50.0176	49.9452	-22.4	-64.8	-0.45	-1.30
	100.1054	99.9073	-24.6	-132.7	-0.25	-1.33
	200.2521	199.9691	102.1	-150.9	0.51	-0.75
mean	49.9994	50.0238	-40.6	13.8	-0.8118	1.00
	100.0711	100.0110	-58.9	-29.0	-0.59	-0.29
	200.1536	200.0166	3.6	-103.4	0.02	-0.52

Table 4. Properties of fibres used in the direct tension tests.

Fibre codification	Coating material	Mode field diameter at 1310 nm	Manufacturer / Reseller
FA01	acrylate	9.2. µm	Huber & Suhner AG, CH
FP01a and FP01b	polyimide	5.2 µm	LUNA Inc, Roanoke VA, US
FP02	polyimide	9.8 µm	Fibrecore, Southhampton, UK

Table 5. Strains measured in different sections of specimens in the direct tension tests L and E at F=72 kN; mean fibre optical strains within each section at front (ε_{FO}^{front}) and back side (ε_{FO}^{back}); average of front and back side fibre optical strains (ε_{FO}^{mean}); DIC strains at front side ($\varepsilon_{DIC}^{front}$); calculated theoretical strain assuming linear elastic behaviour (ε_{th}).

b [mm]	Fibre	ε_{FO}^{front} [µm/m]	$\varepsilon_{DIC}^{front}$ [µm/m]	$\varepsilon_{FO}^{front}-\varepsilon_{DIC}^{front}$ [µm/m]	ε_{FO}^{back} [µm/m]	ε_{FO}^{mean} [µm/m]	ε_{th} [µm/m]	$\varepsilon_{FO}^{mean}-\varepsilon_{th}$ [µm/m]
Specimen L								
30	FA	1970	1967	**3**	-	-	1905	**-**
	FP1a	2041		**74**	2046	2044		**139**
	FP1b	2001		**34**	1989	1995		**90**
	FP2	2048		**81**	2013	2031		**126**
37.5	FA	1724	1641	**83**	1549	1637	1524	**113**
	FP1a	1668		**27**	1495	1581		**57**
	FP1b	1682		**41**	1527	1605		**81**
	FP2	1668		**27**	1513	1591		**67**
50	FA	1329	1295	**34**	1089	1209	1143	**66**
	FP1a	1320		**25**	1031	1176		**33**
	FP1b	1340		**45**	1084	1212		**69**
	FP2	1322		**27**	1057	1190		**47**
Specimen E								
30	FA	2013	2034	**-21**	2026	2019	1905	**114**
	FP1a	2080		**46**	2095	2087		**182**
	FP1b	2047		**13**	2085	2066		**161**
	FP2	2034		**0**	2084	2059		**154**
37.5	FA	1715	1772	**-57**	1548	1631	1524	**107**
	FP1a	1770		**-2**	1638	1704		**180**
	FP1b	1702		**-70**	1566	1634		**110**
	FP2	1724		**-48**	1609	1666		**142**
50	FA	1207	1298	**-91**	1146	1177	1143	**34**
	FP1a	1305		**7**	1251	1278		**135**
	FP1b	1239		**-59**	1184	1212		**69**
	FP2	1260		**-38**	1227	1243		**100**

Table 6. Material properties of the reinforcement used in the panel tests FODIC-10-6 and FODIC-10-8.

Diameter [mm]	Steel type [-]	Yield stress f_s [MPa]	Ultimate Stress f_t [MPa]	Strain at peak load A_{gt} [‰]
Ø6	B500A	505	535	31
Ø8	B500B	522	574	36
Ø10	B500B	519	584	36

Figures

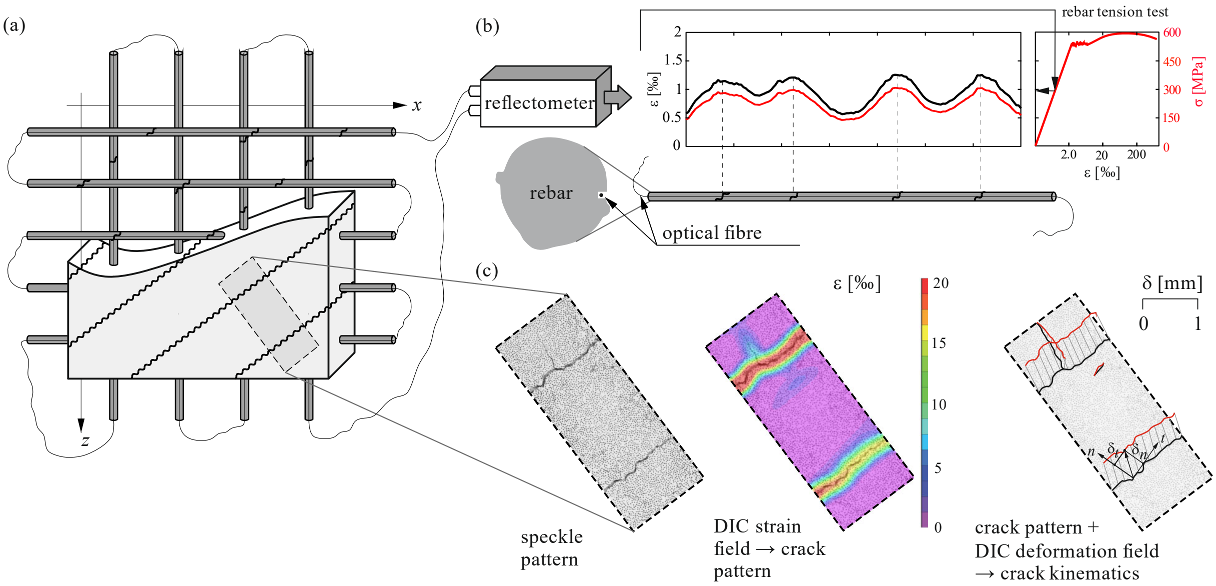

Figure 1. Combined use of digital image correlation (DIC) and distributed fibre optical strain instrumentation (FO): (a) general setup of possible structural concrete experiment with speckled surface and reinforcing bars instrumented with optical fibres; (b) FO continuous strain measurement along one bar and calculation of stresses based on the stress-strain relationship obtained from standard material tensile tests; (c) speckle pattern, strain field obtained with DIC and crack pattern and kinematics computed automatically from the measured DIC strain and deformation fields.

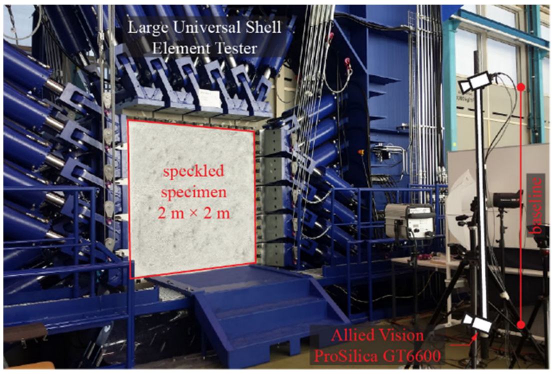

Figure 2. Digital image correlation setup in the Large Universal Shell Element Tester used for the uncertainty quantification in Section 3.1.3.

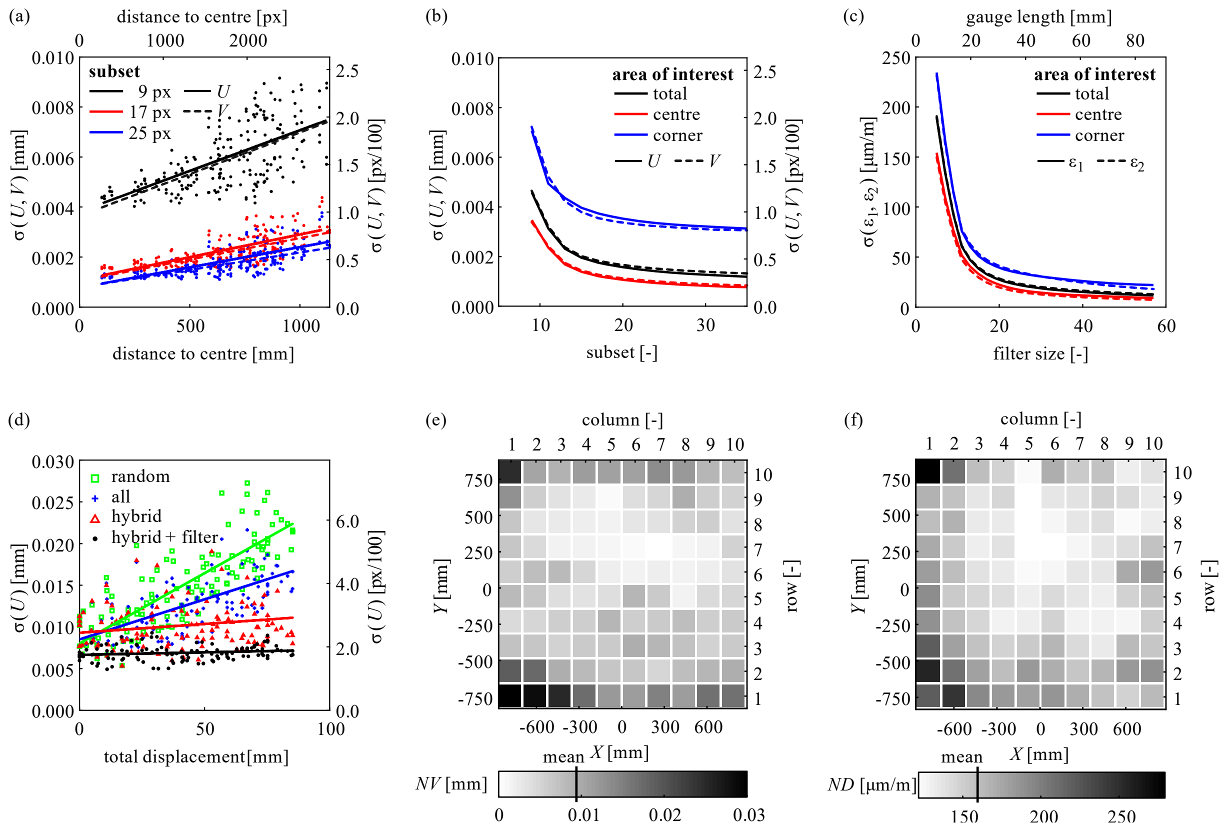

Figure 3. Results of the DIC uncertainty quantification: (a) standard deviation of the displacement in ZDT, dependent on the distance to the image centre; (b) standard deviation of the displacement in ZDT, dependant on the subset size; (c) standard deviation of the principal strains in ZDT, dependent on the filter size; (d) comparison of the measurement error in ZST for different calibrations; (e) benchmark value *NV* for the displacement measurements in ZST according to VDI 2626 [43]; (f) benchmark value *ND* for the strain measurements in ZST according to VDI 2626 [43].

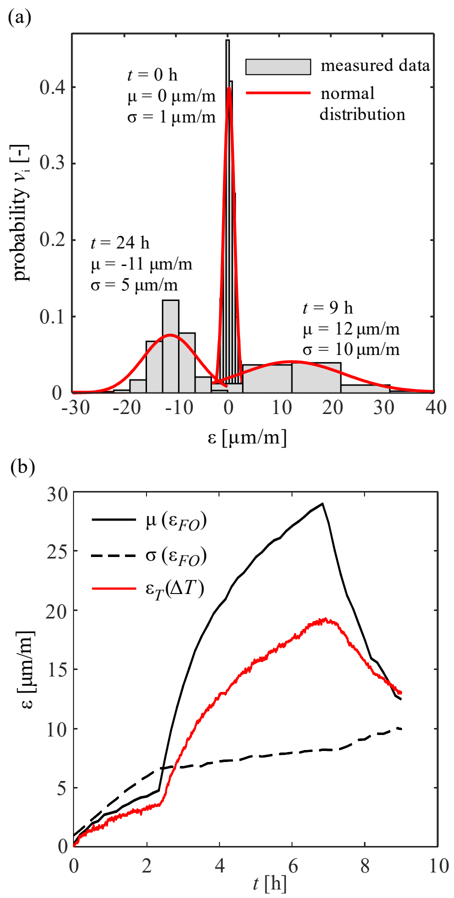

Figure 4. Fibre optical strain measurements on a stationary fibre: (a) histograms and fitted normal distributions (red) of three measurements at different times; (b) evolution over time of mean ($\mu(\varepsilon_{FO})$) and standard deviation ($\sigma(\varepsilon_{FO})$) of strains along the entire fibre, together with the calculated strains due to temperature ($\varepsilon_T(\Delta T)$).

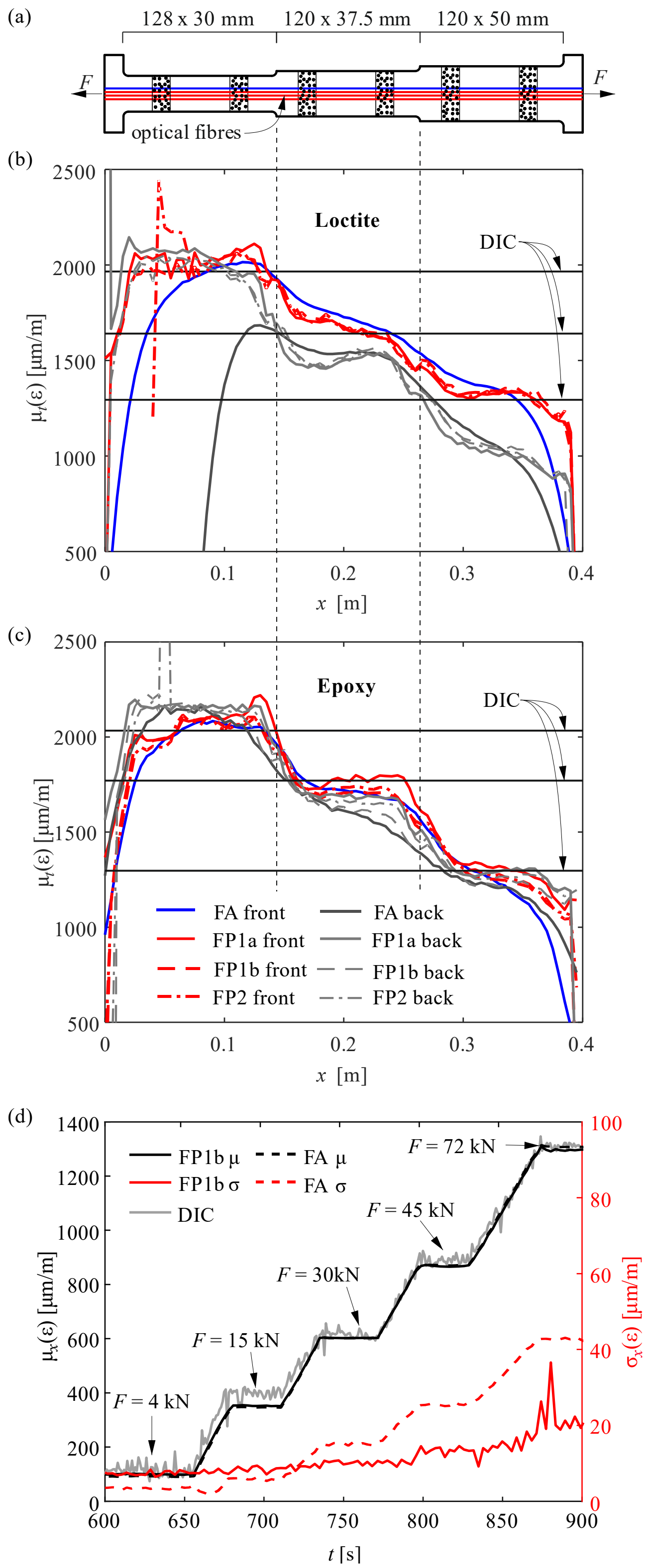

Figure 5. Fibre optical strain measurements on two direct tension tests. Fibres of various types were glued with two different adhesives: (a) geometry of specimens with fibre optical and DIC instrumentation; (b) measured fibre optical and DIC strains over length for specimen with epoxy-glued fibres at 72 kN; (c) measured fibre optical and DIC strains over length for specimen with Loctite-glued fibres at 72 kN; (d) evolution over time of mean strains and standard deviation in the 50 mm wide section for specimen with Loctite-glued fibres, together with DIC strains.

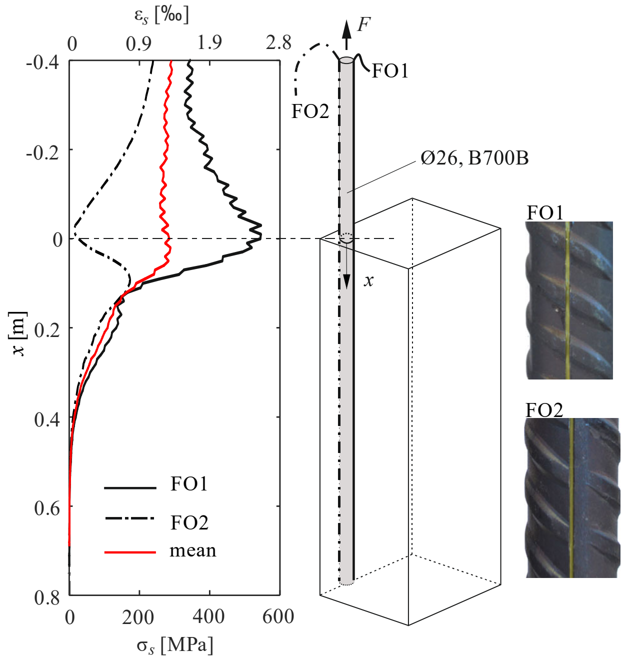

Figure 6. Local phenomena in reinforcing bars observed with fibre optical strain sensors in a pull-out test. Left: measured strains and corresponding stresses of fibres FO1 and FO2 (black) placed opposite to each other, together with their mean value (red); right: geometry of the reinforcing bar with the installed fibres.

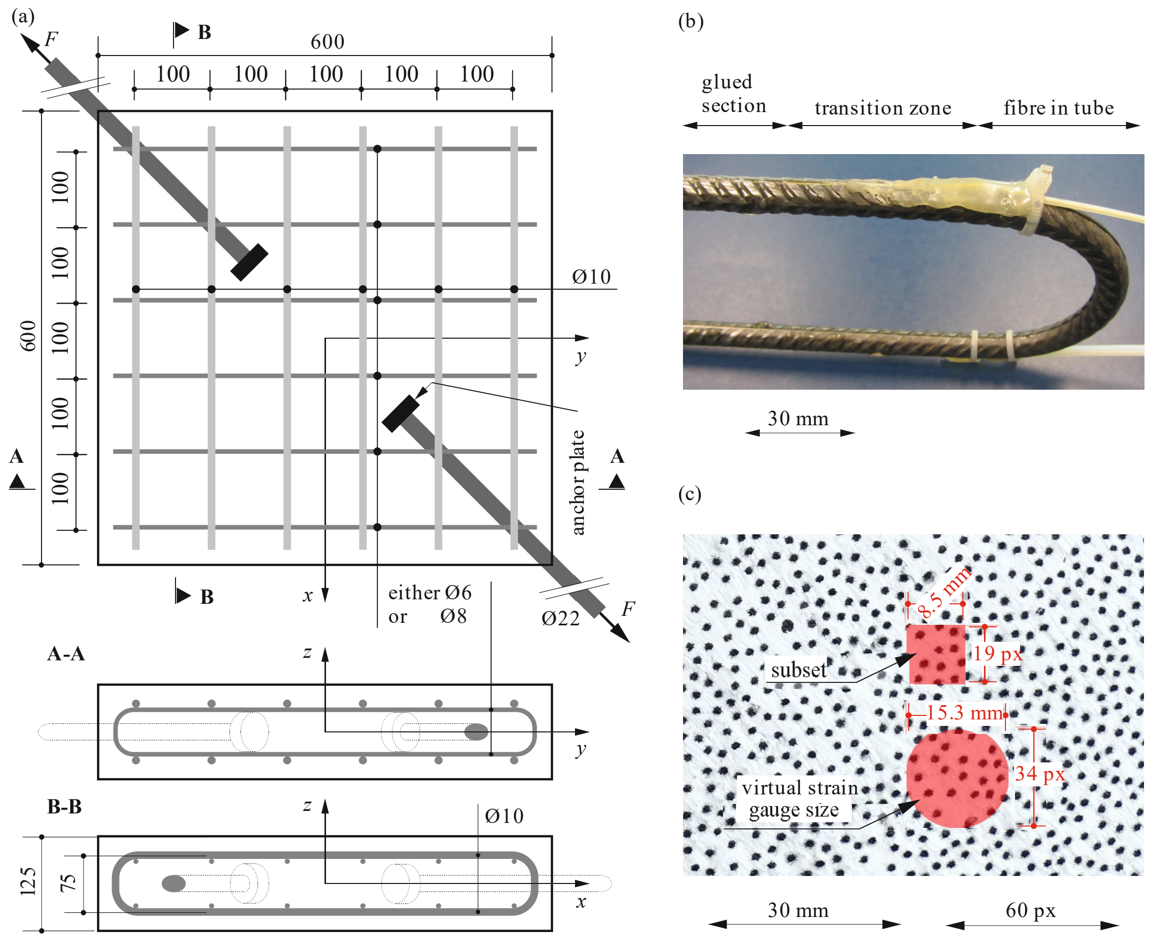

Figure 7. Setup of panel tests FODIC-10-6 and FODIC-10-8: (a) Geometry and reinforcement layout of the specimens (dimensions in [mm]); (b) optical fibre (yellow) in groove of stirrup Ø10 leaving the glued section and continuing in tube; (c) applied speckle on concrete surface for DIC measurements with main parameters of the correlation.

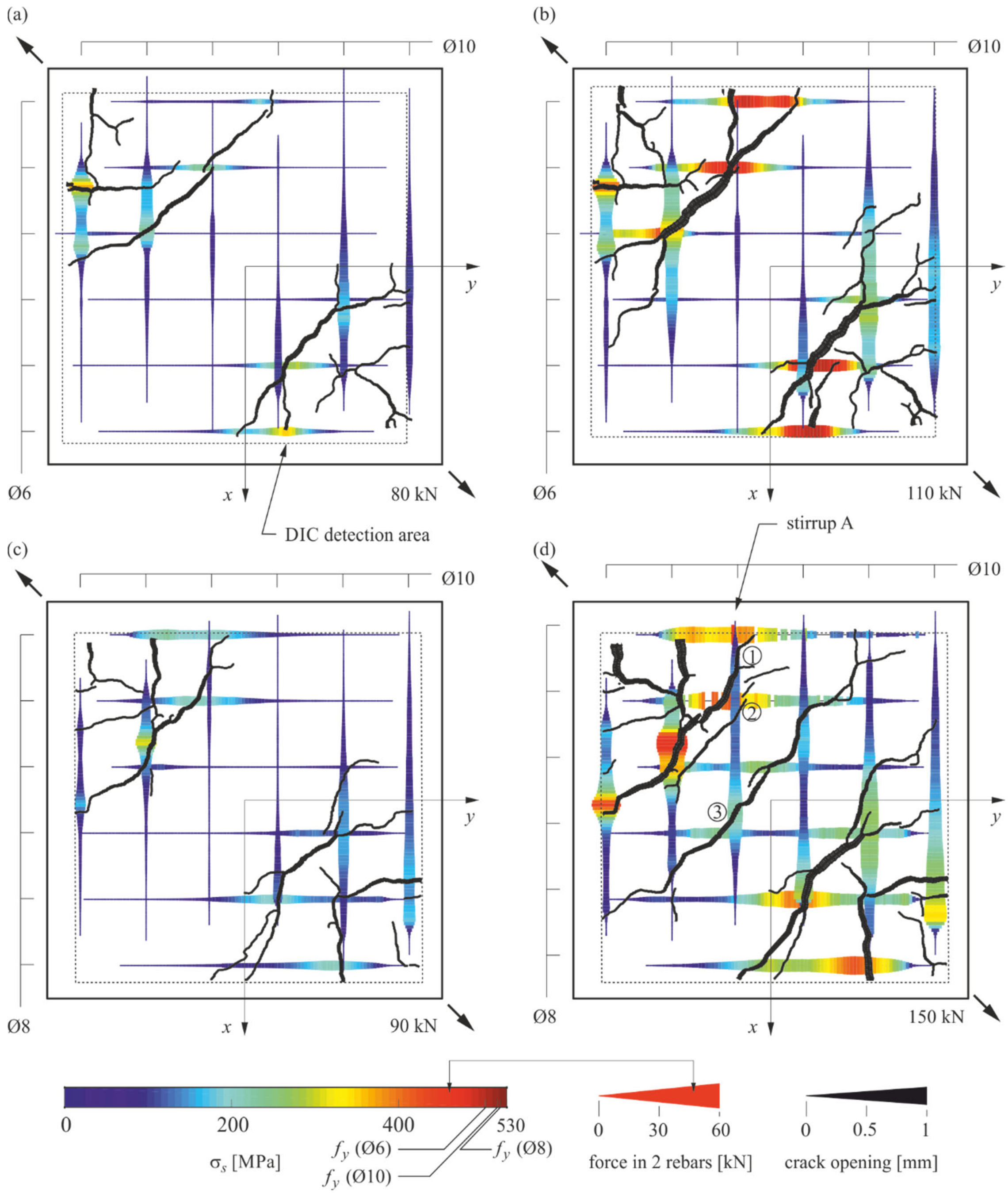

Figure 8. Combined results of fibre optical and DIC measurements: Crack locations and openings together with steel stresses in the front layer and stirrup forces for FODIC-10-6 at (a) 80 kN and (b) 110 kN; for FODIC-10-8 at (c) 90 kN and (d) 150 kN.

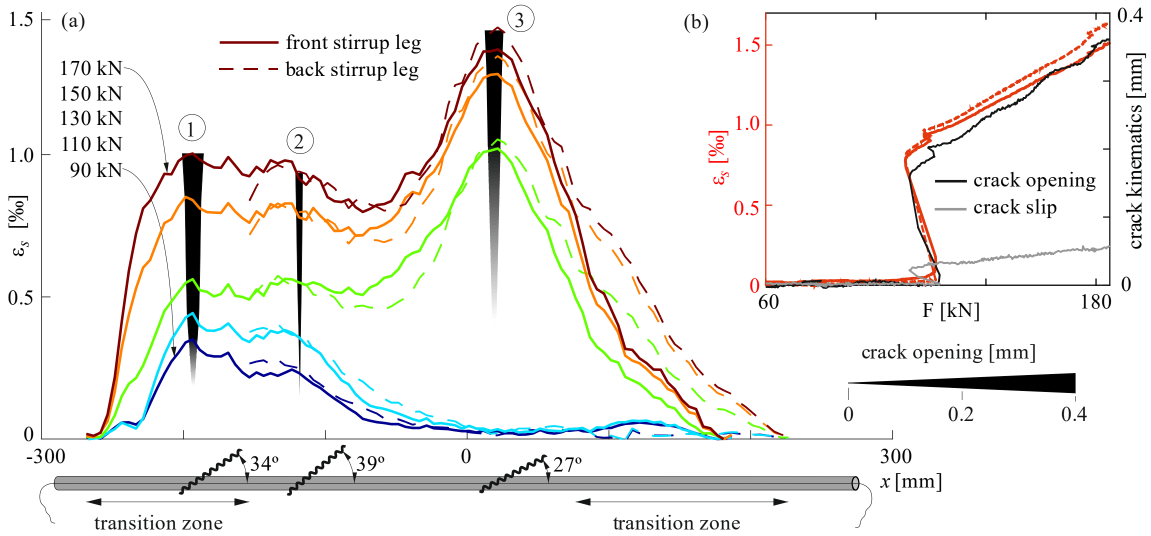

Figure 9. Results of steel strains and crossing cracks for stirrup A (Ø10, y = -50 mm) for FODIC-10-8: (a) measured strains for different load steps with position, orientation and opening of cracks; (b) continuous results over time for crack 3 (x = 20 mm).

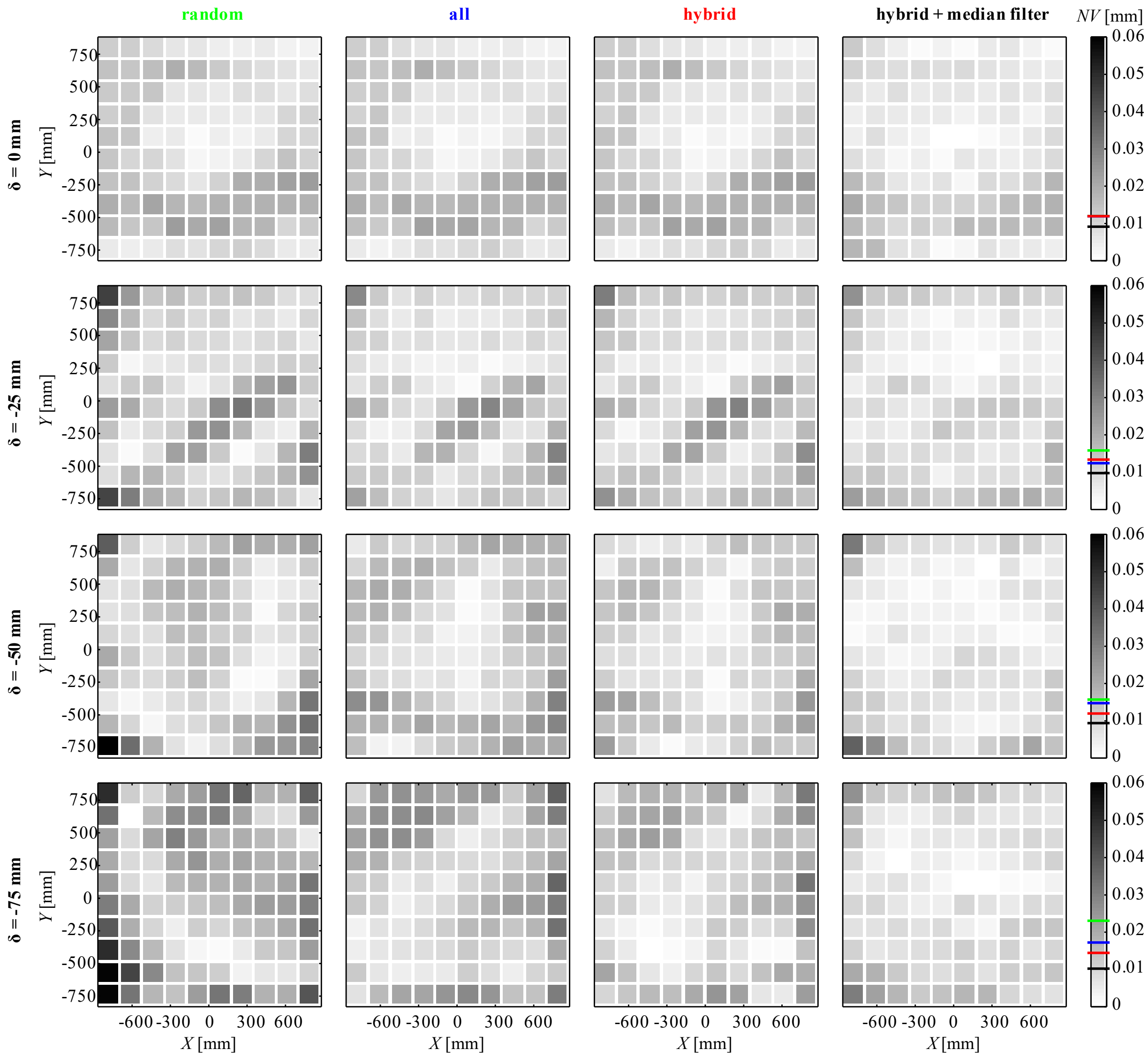

Figure A.1. Results of the DIC uncertainty quantification: uncertainty value *NV* of the displacements in ZST according to VDI 2626 [43] for different calibrations and applied displacements.

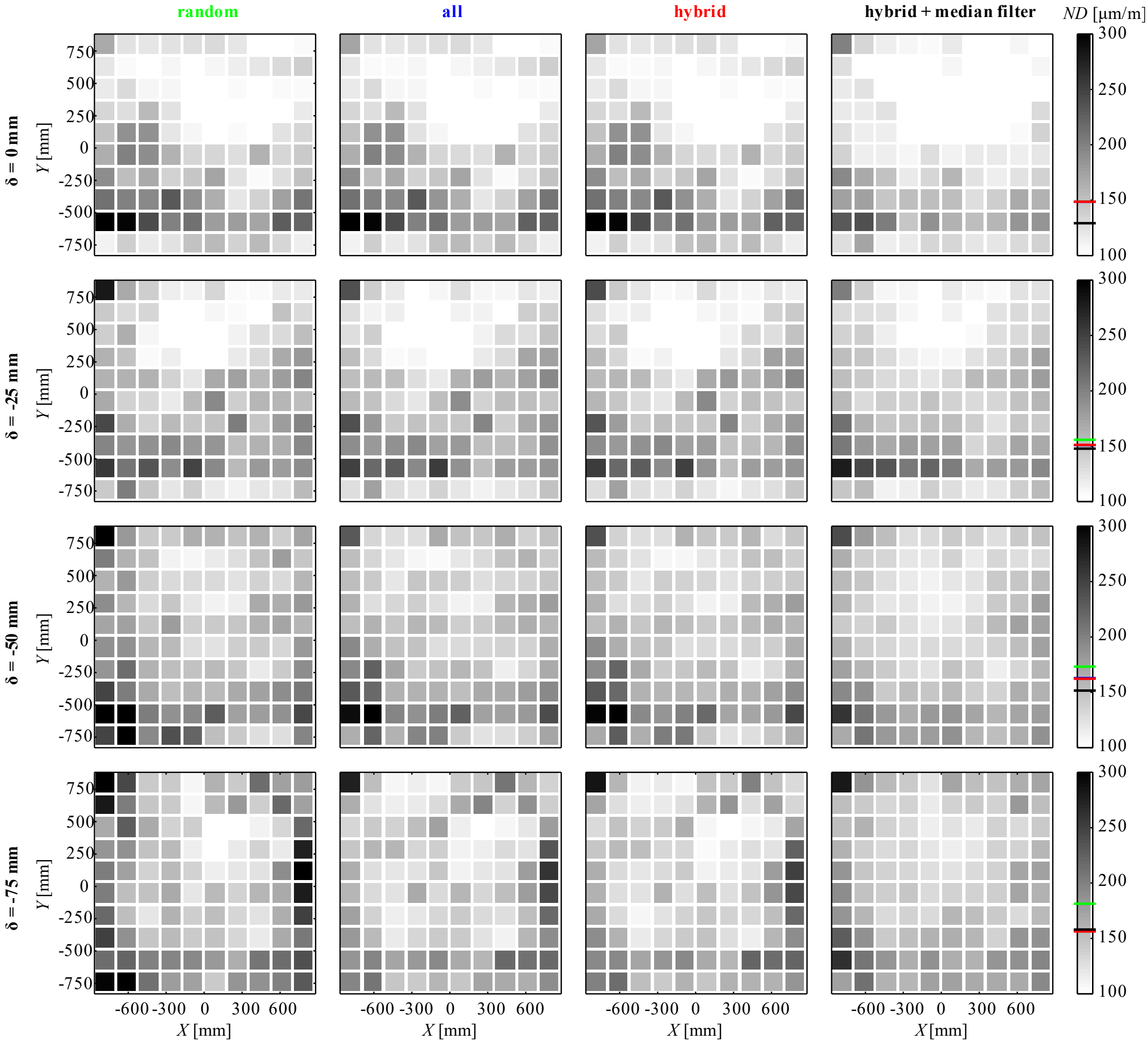

Figure A.2. Results of the DIC uncertainty quantification: uncertainty value *ND* for the full field strain measurements in ZST according to VDI 2626 [43] for different calibrations and applied displacements.